



**HAL**  
open science

## Dynamic Lone Pairs and Fluoride-Ion Disorder in Cubic-BaSnF<sub>4</sub>

Briséis Mercadier, Samuel Coles, Mathieu Duttine, Christophe Legein,  
Monique Body, Olaf Borkiewicz, Oleg Lebedev, Benjamin Morgan, Christian  
Masquelier, Damien Dambournet

► **To cite this version:**

Briséis Mercadier, Samuel Coles, Mathieu Duttine, Christophe Legein, Monique Body, et al.. Dynamic Lone Pairs and Fluoride-Ion Disorder in Cubic-BaSnF<sub>4</sub>. *Journal of the American Chemical Society*, 2023, 145 (43), pp.23739-23754. 10.1021/jacs.3c08232 . hal-04250709

**HAL Id: hal-04250709**










**<https://hal.science/hal-04250709>**

Submitted on 19 Oct 2023

**HAL** is a multi-disciplinary open access archive for the deposit and dissemination of scientific research documents, whether they are published or not. The documents may come from teaching and research institutions in France or abroad, or from public or private research centers.

L'archive ouverte pluridisciplinaire **HAL**, est destinée au dépôt et à la diffusion de documents scientifiques de niveau recherche, publiés ou non, émanant des établissements d'enseignement et de recherche français ou étrangers, des laboratoires publics ou privés.

# Dynamic Lone Pairs and Fluoride-Ion Disorder in Cubic-BaSnF<sub>4</sub>

Briséis Mercadier<sup>†</sup> <sup>1,2,3</sup> Samuel W. Coles<sup>†</sup> <sup>4,5</sup> Mathieu Duttine <sup>6</sup>  
Christophe Legein <sup>7</sup> Monique Body <sup>7</sup> Olaf J. Borkiewicz <sup>8</sup> Oleg Lebedev,<sup>9</sup>  
Benjamin J. Morgan\* <sup>4,5</sup> Christian Masquelier <sup>1,3</sup> and Damien Dambournet\* <sup>1,2</sup>

<sup>1</sup>Réseau sur le Stockage Electrochimique de l'Energie,  
RS2E, FR CNRS 3459, 80039 Amiens Cedex, France

<sup>2</sup>Sorbonne Université, CNRS, Physicochimie des Electrolytes et  
Nanosystèmes Interfaciaux, UMR CNRS 8234, 75005 Paris, France

<sup>3</sup>Laboratoire de Réactivité et de Chimie du Solides,  
UMR CNRS 7314, 80039 Amiens Cedex, France

<sup>4</sup>Department of Chemistry, University of Bath, Claverton Down BA2 7AY, United Kingdom

<sup>5</sup>The Faraday Institution, Quad One, Harwell Science and Innovation Campus, Didcot OX11 0RA, United Kingdom

<sup>6</sup>Institut de Chimie de la Matière Condensée de Bordeaux, UMR CNRS 5026, 33608 Pessac, France

<sup>7</sup>Institut des Molécules et Matériaux du Mans, UMR CNRS 6283,  
Le Mans Université, 72805 Le Mans Cedex 9, France

<sup>8</sup>X-ray Science Division, Advanced Photon Source,

Argonne National Laboratory, Illinois 60439, United States

<sup>9</sup>Laboratoire de Cristallographie et Sciences des Matériaux, CRISMAT, 14000 Caen, France

(Dated: September 6, 2023)

**ABSTRACT** Introducing compositional or structural disorder within crystalline solid electrolytes is a common strategy for increasing their ionic conductivity. (M,Sn)F<sub>2</sub> fluorites have previously been proposed to exhibit two forms of disorder within their cationic host frameworks: occupational disorder from randomly distributed M and Sn cations, and orientational disorder from Sn(II) stereoactive lone pairs. Here, we characterise the structure and fluoride-ion-dynamics of cubic-BaSnF<sub>4</sub>, using a combination of experimental and computational techniques. Rietveld refinement of XRD data confirms an average fluorite structure with {Ba,Sn} cation disorder, and the <sup>119</sup>Sn Mössbauer spectrum demonstrates the presence of stereoactive Sn(II) lone pairs. X-ray total-scattering PDF analysis and *ab initio* molecular dynamics simulations reveal a complex local structure with a high degree of intrinsic fluoride-ion disorder, where 1/3 of fluoride ions occupy octahedral “interstitial” sites: this fluoride-ion disorder is a consequence of repulsion between Sn lone pairs and fluoride ions that destabilises Sn-coordinated tetrahedral fluoride-ion sites. Variable-temperature <sup>19</sup>F NMR experiments and analysis of our molecular dynamics simulations reveal highly inhomogeneous fluoride-ion dynamics, with fluoride ions in Sn-rich local environments significantly more mobile than those in Ba-rich environments. Our simulations also reveal dynamical reorientation of the Sn lone pairs that is biased by the local cation configuration and is coupled to the local fluoride-ion dynamics. We end by discussing the effect of host-framework disorder on long-range diffusion pathways in cubic BaSnF<sub>4</sub>.

## INTRODUCTION

The ability of solid electrolytes to allow ion transport in the solid state makes them useful for a range of applications, including fuel cells and solid-state batteries [1–5]. As a consequence, a considerable amount of research has focussed on understanding how the structure and chemical composition of particular solid electrolytes modulate their ionic conductivity [3, 6–13]. In addition to providing insight into the atomic-scale mechanisms of ionic conductivity within specific families of solid electrolytes, this body of research has also produced various “design principles”—general conceptual models that seek to explain, and predict, trends in ionic conductivity across different families of solid electrolytes [8, 12, 14–19]. Many of these solid electrolyte design principles reflect how changes to the structure and composition of the host framework—the set of non-diffusive ions within a solid electrolyte—modulate the potential energy surface for the mobile ions, and hence influence overall ionic

conductivity [6, 11, 16, 19–21].

One such design principle arises from the observation that solid electrolytes with some form of host-framework disorder often have significantly higher ionic conductivities than related compounds with well-ordered host frameworks [10, 15, 22–30]. Framework-disordered solid electrolytes typically exhibit one of two classes of disorder: occupational disorder, where two or more distinct species occupy the same crystallographic positions [10, 15, 24, 28, 29, 31–36]; or orientational disorder, where molecular or polyatomic subunits within the host framework have different disordered orientations [37–40]. Orientational disorder can be static, where each polyatomic subunit has a fixed average orientation over experimentally relevant timescales [41, 42], or dynamic, where the polyatomic subunits rotate and reorient [40, 43, 44]. In some solid electrolytes, this reorientational dynamics of the host framework is thought to couple to the diffusive dynamics of the mobile ion species, giving rise to a so-called “paddlewheel” effect [21, 38, 43, 45].

While orientational disorder in solid electrolytes is usually discussed in the context of molecular or polyanion orientational degrees of freedom, materials that contain post-transition metals with “stereoactive” lone pairs; such as Sn or Bi; may exhibit *electronic* orientational disorder [46]. These cations, when in an oxidation state two less than their formal maximum (e.g., Sn<sup>II</sup> and Bi<sup>III</sup>), have a formal electron configuration with a filled *s*-orbital as their last valence shell. These *s*<sup>2</sup> states can mix with neighbouring-anion *p* states to form a bonding state and an antibonding state, and this antibonding state mixes with metal *p* states to form an asymmetric lone pair state, characterised by an eccentric (off-center with respect to the atomic nucleus) “stereoactive” charge density, that directs the cation coordination geometry and often results in distorted low-symmetry cation coordination environments [47, 48].

In many materials that contain stereoactive lone pairs, the local distortions due to these lone pairs are correlated over long length scales. These materials are long-range ordered and their structures can be determined using average crystallographic techniques such as Bragg diffraction. In other materials, however, the distortions due to stereoactive lone-pairs are uncorrelated [46, 49, 50]. These materials are crystallographically disordered and average-structure crystallographic methods yield inaccurate high-symmetry structural models. Because the distortion around each cation depends on the relative orientation of the corresponding lone pair, this behaviour can be considered a form of orientational disorder, analogous to molecular or polyanionic orientational disorder as discussed above. These lone-pair effects may also be dynamic, showing fluctuations [46, 51–53] or even rotations [54, 55] of the lone-pair charge density, mirroring the dynamic orientational disorder of “paddlewheel” materials [21, 38, 45].

While the role of stereoactive lone-pairs in solid electrolytes has previously been discussed in the context of crystallographically ordered materials [56–60], a detailed understanding of lone-pair behaviour and its effect on ion transport in crystallographically disordered solid electrolytes is currently lacking [61–63].

Here, we report a combined experimental and computational study of the fluorite-structured fluoride-ion conductor, cubic (c-)BaSnF<sub>4</sub>. We find that c-BaSnF<sub>4</sub> exhibits both site-occupational disorder, due to Ba/Sn cation mixing, and dynamic orientational disorder, due to Sn stereoactive lone pairs. The combination of these two forms of host-framework disorder within an ion-conducting material makes c-BaSnF<sub>4</sub> a particularly interesting focus of study. We show that these two forms of disorder are coupled and that together they strongly influence the structure and dynamics of the mobile fluoride ions. The fluoride ion substructure is highly disordered, with 1/3 of fluoride ions occupying “interstitial” sites, due to lone-pair repulsion of fluoride ions in highly tin-coordinated sites. Fluoride ion dynamics are strongly dependent on the local cation environment and are cou-

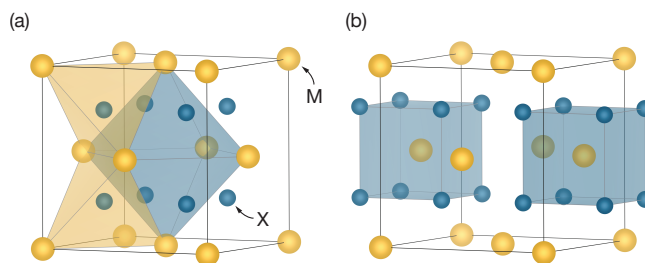


FIG. 1. Schematic of the MX<sub>2</sub> fluorite structure (space group *Fm*3*m*), highlighting (a) tetrahedral (normal; Wyckoff 8c) and octahedral (interstitial; Wyckoff 4b) anion sites and (b) cubic cation sites (Wyckoff 4a).

pled to dynamical reorientations of neighbouring Sn lone pairs. Our study provides new insight into the rich structural and dynamical behaviour of fluoride-ion conducting c-BaSnF<sub>4</sub> and how this arises from the unusual combination of coupled site-occupation and lone-pair-orientation host framework disorder.

### Cation disorder and stereoactive lone pairs in F-ion-conducting fluorites

The study of fluoride-ion-conducting fluorites has a long history, starting from Faraday’s discovery of superionic  $\beta$ -PbF<sub>2</sub> [64]. More recently, this family of materials have been the subject of renewed interest because of their potential use as electrolytes in solid-state fluoride-ion batteries [65–68].

The fluorite structure is comprised of a face-centered-cubic cation lattice, with anions occupying all of the tetrahedral holes (Fig. 1(a)). The octahedral holes are vacant, and are usually considered as “interstitial” sites. An alternative structural description is obtained by considering the positions of cations within an anionic substructure (Fig. 1(b)): from this perspective, the anions define a simple-cubic lattice, and the cations occupy half the cubic holes, giving 8-fold MX<sub>8</sub> cation coordination.

In conventional fluorites, such as CaF<sub>2</sub>, anion transport requires the presence of thermally-generated point defects—vacancies and interstitials—within the anionic substructure [69–72]. Fluorites are typically anti-Frenkel disordered: some fraction of anions occupy octahedral interstitial sites, leaving an equal number of tetrahedral sites vacant [69]. While additional interstitials and vacancies can be introduced via aliovalent doping, the intrinsic defect concentration depends on the ease with which anti-Frenkel pairs can form, which, in turn, approximately depends on the relative energies of ions occupying the tetrahedral and octahedral anion sites within the fcc cationic host framework. In simple fluorites, the anti-Frenkel-pair formation energy is usually high: for CaF<sub>2</sub>, anion Frenkel-pair formation energies have been calculated as 2.2 eV to 2.9 eV [69, 73–75]. As a consequence, at low-to-moderate temperatures, these materi-

als have low fluoride-ion defect concentrations and corresponding low ionic conductivities [56, 76].

Significantly higher ionic conductivities are found in fluorite-structured materials that contain cations with stereoactive lone pairs, such as  $\beta$ -PbF<sub>2</sub> [56, 76, 77]. This effect has been suggested to be a possible consequence of the high polarisability of the cation facilitating diffusion of the mobile anions [56, 77, 78], or that the negative charge of the Pb lone pairs might electrostatically destabilise adjacent fluoride ions in tetrahedral sites, thereby promoting the formation of anti-Frenkel pairs [56]. Neutron diffraction data [79] and AIMD simulations [80] of  $\beta$ -PbF<sub>2</sub>, however, show no evidence for octahedral site occupation by fluoride ions, bringing into question the hypothesis that the presence of stereoactive lone pairs in fluorite-structured materials promotes Frenkel pair formation [81].

A second class of fluorite-structured materials that exhibit particularly high ionic conductivities are disordered mixed-cation systems,  $M'_xM''_{1-x}F_2$  [24, 33, 77, 82–85]. The highest ionic conductivity materials in this class are those with different valence cations, such as RbBiF<sub>4</sub>, where cation disorder induces high levels of anion disorder [83, 86]. A significant increase in ionic conductivity compared to analogous single-cation fluorites is also observed for mixed-cation systems where both cations have a formal 2+ oxidation state, such as Ba<sub>1-x</sub>Ca<sub>1+x</sub>F<sub>2</sub> [24, 25, 33]: again, the presence of cation disorder causes considerable fluoride disorder where fluoride ions displaced significantly from their ideal crystallographic positions to form “pseudovacancies” [24].

Some fluorite materials exhibit both stereoactive lone pairs and cation mixing [62, 86–89]. Of particular relevance to the present study is the work of Dénès *et al.* on Ca<sub>1-x</sub>Sn<sub>x</sub>F<sub>2</sub> ( $x = 0.27$ ) [62, 87]. For this system, X-ray diffraction (XRD) data give a cubic fluorite average structure, consistent with a solid solution of Ca and Sn distributed randomly over the cation positions, and <sup>119</sup>Sn Mössbauer data show a large quadrupole doublet, characteristic of a stereoactive tin lone pair.

The presence of a stereoactive tin lone pair requires an asymmetric tin coordination environment, which is inconsistent with the structural model implied by the diffraction data, in which Ca and Sn both have cubic MF<sub>8</sub> coordination (cf. Fig. 1(b)). To reconcile these apparently contradictory data, Dénès and coworkers proposed a structural model wherein each tin is displaced towards one face of the enclosing [F8] cube to give square-pyramidal SnF<sub>4</sub>E coordination, where E denotes the stereoactive lone pair, with this lone pair oriented towards the more distant [F8] cube face. These tin lone pairs then are assumed to orient randomly along each possible  $\langle 100 \rangle$  direction to give an average structure with cubic symmetry, consistent with the experimental diffraction data.

The structural model proposed by Dénès *et al.* implies that Ca<sub>1-x</sub>Sn<sub>x</sub>F<sub>2</sub> exhibits both occupational cation disorder and Sn lone-pair orientational disorder, and similar

behaviour might be expected in other mixed-cation fluorites where one cation species has a stereoactive lone pair [88, 89]. Such mixed-cation fluorites are interesting to examine in the context of understanding how these distinct but coexisting forms of host-framework disorder together modulate the structure and dynamics of the mobile anion species. Here, we focus on the structure and fluoride-ion dynamics of c-BaSnF<sub>4</sub>, which we consider a representative member of this family of mixed-cation fluorites. c-BaSnF<sub>4</sub> is also of practical interest due to its shared composition with the more widely-studied layered tetragonal phase t-BaSnF<sub>4</sub> [60, 90, 91], which is considered to be a prospective solid electrolyte for fluoride-ion batteries [92, 93].

## MATERIALS AND METHODS

*Synthesis* Cubic BaSnF<sub>4</sub> was synthesized via a ball-milling process, using a planetary mill (Fritsch Pulverisette 6). Precursors (SnF<sub>2</sub>, Sigma-Aldrich, 99%; BaF<sub>2</sub>, Sigma-Aldrich 99.99%) were dried at 150 °C under vacuum for 3 h, and stored under Ar inert atmosphere. The desired amounts of precursors were weighed and sealed in Zirconia milling jars in an argon-filled glove box, with a powder to ball ratio of 1:13. The balls were 10 mm in diameter and made out of zirconia. The precursors were then milled at 400 rotations/min for 12 hours, divided into 24 cycles. Each cycle consisted of 15 minutes of milling and 15 minutes of pause, which prevented overheating.

*Impedance Spectroscopy* Electrochemical Impedance spectroscopy was performed on c-BaSnF<sub>4</sub> powder pressed into a pellet. Gold was sputtered on both sides of the pellet to guarantee good contact. A BioLogic MTZ-35 impedance analyzer was used to collect data in a frequency range of  $3.5 \times 10^7$  Hz to 1 Hz, under Ar atmosphere. The resulting data were fitted using the equivalent circuit model proposed in Ref. [94].

*X-Ray Diffraction* X-ray diffraction was performed using a Bruker D8 Advance powder diffractometer, with a copper anode (Cu-K<sub>α</sub> = 1.540 59 Å). The powder XRD pattern was fitted using the Rietveld method as implemented in the FULLPROF program [95], with a split-pseudo-Voigt function to model the peaks [96].

*<sup>119</sup>Sn Mössbauer Spectroscopy* A lab-made constant acceleration Halder-type spectrometer operating in transmission geometry was used to carry out the Mössbauer analyses. The spectrometer was equipped with a radioactive source of <sup>119m</sup>Sn (370 MBq) embedded in a CaSnO<sub>3</sub> matrix and maintained at room-temperature. Experiments were performed with 50 mg to 70 mg of sample ( $[\text{Sn}] = 5 \text{ mg cm}^{-2}$  to  $8 \text{ mg cm}^{-2}$ ) at room temperature ( $\sim 293$  K) and 77 K using a liquid nitrogen bath cryostat. The Mössbauer hyperfine parameters ( $\delta$  isomer shift,  $\Delta$  quadrupole splitting,  $\Gamma$  signal linewidth,  $G_{11}$  Goldanskii-Karyagin factor and relative areas) were refined using the WINNORMOS software [97]. Isomer-shift values are

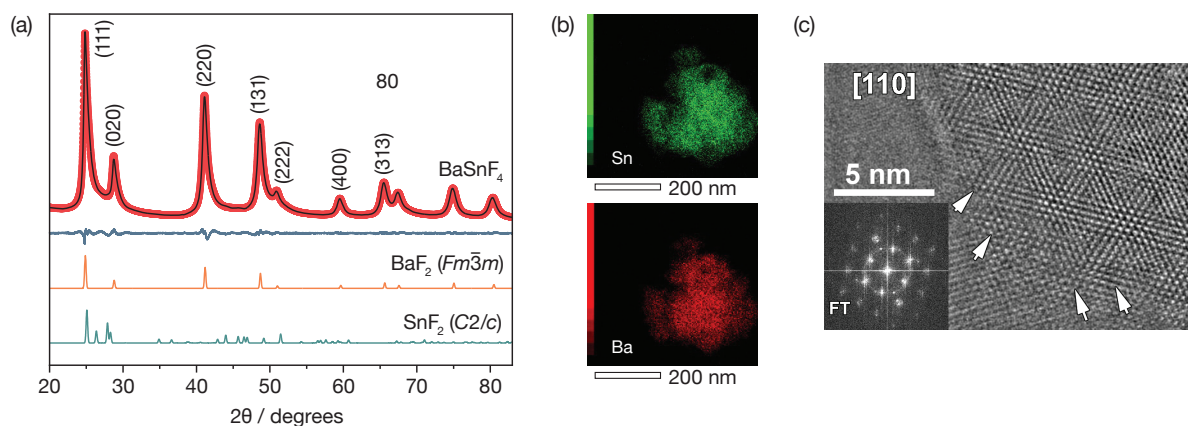


FIG. 2. (a) Powder XRD pattern and Rietveld analysis of *c*-BaSnF<sub>4</sub>. Reference patterns of the BaF<sub>2</sub> and SnF<sub>2</sub> precursors are presented at the bottom of the panel. (b) Distribution of barium (red; left panel) and tin (green; right panel) within a *c*-BaSnF<sub>4</sub> particle, seen via EDX-mapping. (c) HRTEM image of *c*-BaSnF<sub>4</sub>.

reported relative to CaSnO<sub>3</sub> at room temperature.

**<sup>19</sup>F Solid-State NMR** Quantitative <sup>19</sup>F Magic Angle Spinning (MAS) NMR spectra were recorded on Bruker Avance III spectrometers operating at  $B_0 = 7.0$  T (<sup>19</sup>F Larmor frequency of 282.4 MHz), using a 1.3 mm CP-MAS probe head, and, for variable temperature experiments, using a 2.5 mm double resonance (<sup>1</sup>H/<sup>19</sup>F-X) CP-MAS probe and a Bruker Cooling Unit (BCU-II). The <sup>19</sup>F MAS spectra were recorded using a Hahn echo sequence with an interpulse delay equal to one rotor period. The 90° pulse lengths were set to 1.25 μs (for SnF<sub>2</sub> and BaSnF<sub>4</sub>) and 1.5 μs (BaF<sub>2</sub>) and the recycle delays were set to 900 s (for SnF<sub>2</sub>) and 300 s (for BaF<sub>2</sub> and BaSnF<sub>4</sub>) using the 1.3 mm CP-MAS probe head. For the variable-temperature experiments, using the 2.5 mm CP-MAS probe head, the 90° pulse length was set to 2 μs and the recycle delay was set to 10 s. The temperature inside the rotor was estimated from the chemical shift and spin-lattice relaxation time ( $T_1$ ) of <sup>79</sup>Br in KBr powder [98]. <sup>19</sup>F spectra are referenced to CFCl<sub>3</sub> and were fitted using the DMFIT software [99].

**Pair-Distribution Functions** Pair-distribution function (PDF) measurements were performed at the 11-ID-B beamline at the Advanced Photon Source at Argonne National Laboratory. High-energy synchrotron XRD ( $\lambda = 0.2128$  Å) 2D total scattering data was collected and integrated into one-dimensional diffraction data using FIT2D [100]. The PDFGETX3 software was used to carry out Fourier transformation and correction of the PDFs [101]. Refinements were performed using the software PDFGUI [102].

**Molecular-Dynamics Simulations** To model the equilibrium structure and dynamics of *c*-BaSnF<sub>4</sub>, we performed *ab initio* molecular dynamics (AIMD) using the Vienna *ab initio* simulation package (VASP) [103–105]. We used the revised Perdew–Burke–Ernzerhof generalized gradient approximation PBEsol exchange–correlation function [106]. Interactions between core and

valence electrons were described within the projector-augmented-wave (PAW) method [107], with cores of [Kr] 4d<sup>10</sup> for Ba, [Kr] for Sn, and [He] for F. We simulated a  $6 \times 6 \times 6$  supercell, starting from a cation-disordered fluorite structure with a special-quasi-random configuration of Ba and Sn over the Wyckoff 4a cation sites, that we generated using the ICET package [108]. This  $6 \times 6 \times 6$  special-quasi-random structure best approximates the Ba/Sn correlations for an infinite lattice with a fully-random arrangement of cations [109, 110].

Our molecular dynamics simulation used a plane-wave cutoff of 350 eV with only the gamma point used for  $k$ -space sampling, and without spin-polarisation. The simulation was performed at 600 K and used a time-step of 2 fs. Before our production run, we obtained the 600 K equilibrium volume by running a preliminary series of simulations with different cell volumes for 8 ps each, and fitting the Birch–Murnaghan equation to the resulting energy–volume dataset. The simulation was run in the *NVT* ensemble using a Nosé–Hoover thermostat. Thermal equilibration was performed by running a 2 ps *NVE* run with temperature rescaling every 50 steps. The production run was 159 ps in length.

To calculate fluoride-ion site occupancies and site–site transition frequencies, at each simulation timestep we assigned every fluoride ion to a distinct tetrahedral or octahedral site by projecting the instantaneous fluoride-ion positions onto polyhedral “sites” defined by the Wyckoff 4a positions as fixed vertex positions (1).

For structural analysis (calculation of radial distribution functions and cation–4a displacements) we extracted a set of “inherent” structures [111–113] from our simulation trajectory by performing a conjugate-gradient geometry optimisation on configurations selected every 50 timesteps. Each inherent structure represents a local minimum on the corresponding 3N-dimensional potential energy surface. To calculate an example electron localisation function (ELF) [114] we performed full geometry

optimisations with a cutoff of 500 eV with a minimum  $k$ -point spacing of  $0.25 \text{ \AA}^{-1}$ , with atomic positions and cell parameters relaxed until all atomic forces were less than  $2 \times 10^{-2} \text{ eV \AA}^{-1}$ .

To obtain tin lone pair orientations, we calculated the set of maximally-localised Wannier functions [115] for structures sampled every 50 ps, using the WANNIER90 code [116]. The net dipole on each tin atom is calculated by associating each Wannier center with the closest ion, and then, for each tin, summing over all associated Wannier-center displacement vectors [117]. We assume that tin polarisation is dominated by contributions from the lone pair states, and that our calculated polarisation vectors therefore characterise these lone pair orientations.

Analysis of the simulation data was performed using the REVELSMD [118], SITE-ANALYSIS [119], ASE [120], PYMATGEN [121], NUMPY [122], and SCIPY [123] codes. The time-average fluorine density (Fig. 6) was calculated using a linear combination of a conventional histogram with a triangular kernel and a force-extrapolated analogue, as described in Refs. [124–126].

## RESULTS AND DISCUSSION

### Structural characterisation

Cubic  $\text{BaSnF}_4$  was synthesised by mechanically milling  $\text{BaF}_2$  and  $\text{SnF}_2$  in a manner similar to Ref. 94 (see Methods). The X-ray diffraction pattern (Fig. 2) indexes to a face-centered cubic structure from the  $Fm\bar{3}m$  (225) space group, consistent with an average fluorite-structure. The X-ray pattern shows no visible peaks for the parent  $\text{SnF}_2$  ( $C2/c$ ) phase, and Energy Dispersive X-ray analysis (EDX-mapping) shows homogeneous distributions for both Sn and Ba. Quantitative analysis of the EDX-mapping data gives proportions of Ba and Sn of 49.6(7) % and 50.3(7) %, respectively, which is close to the nominal 1:1 Ba:Sn stoichiometry (see Fig. S2 for the full mapping data). As a further check on the synthesised compound, we performed electrochemical impedance spectroscopy, and obtained an ionic conductivity at 30 °C of  $4.6 \times 10^{-6} \text{ S cm}^{-1}$ , with an activation energy of 0.56 eV. This ionic conductivity is consistent with previous literature values for  $c\text{-BaSnF}_4$  [94], and is  $> 10^3$  higher than that of fluorite-structured  $\text{BaF}_2$  [24], illustrating the positive effect of cation mixing on fluoride-ion transport.

Our XRD data show no superstructure reflections, indicating that Ba and Sn are disordered over the cation sites. From indexing the XRD data, we obtain a cell parameter of  $a = 6.1945(2) \text{ \AA}$ , which is close to the value for pristine  $\text{BaF}_2$  of  $a = 6.1964(2) \text{ \AA}$  [127]. This result is somewhat unexpected, given the smaller ionic radius of  $\text{Sn}^{2+}$  compared to  $\text{Ba}^{2+}$ , and suggests the possibility of local distortions in the cation substructure. Düvel *et al.* reported similar excess-volume behaviour in  $\text{Ba}_{1-x}\text{Ca}_x\text{F}_2$  solid solutions [24], where this was proposed as a con-

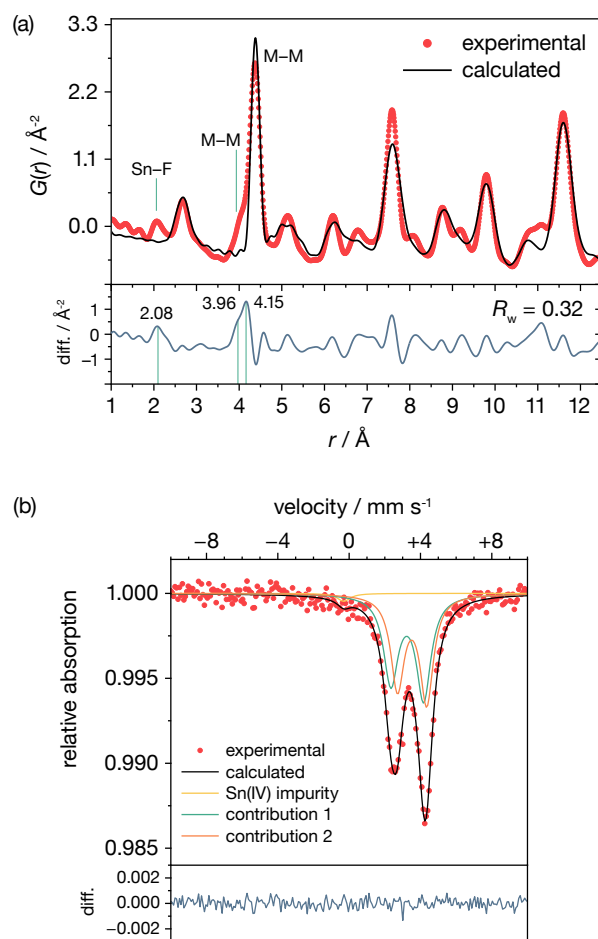


FIG. 3. (a) PDF refinement obtained using a cubic model. The main atomic distances referred to in the main text have been labeled. The green curve shows the difference between calculated and experimental data. (b) Room temperature (293 K)  $^{119}\text{Sn}$  Mössbauer spectrum of  $c\text{-BaSnF}_4$ . Fitting parameters for the two contributions shown are provided in the Supporting Information.

tributing factor to enhanced fluoride-ion transport relative to the end-members. HRTEM data provide further evidence of local deviations from an ideal fluorite-type structure; these show visible changes in inter-reticular distances (Fig. 2c, white arrows) that indicate regions of local strain.

Additional structural information is given by our X-ray total-scattering PDF data. For interatomic distances between 12  $\text{Å}$  and 50  $\text{Å}$ , the PDF data are relatively well described by a cubic fluorite  $Fm\bar{3}m$  model ( $R_w = 20\%$ ; see Fig. S3). At short range, however (between 1  $\text{Å}$  and 12  $\text{Å}$ ; Fig. 3(a)), this high-symmetry structural model gives a poor fit to the PDF data ( $R_w = 32\%$ ), indicating that the local structure of  $c\text{-BaSnF}_4$  deviates significantly from an ideal fluorite-type structure. The cubic model fails to predict the peak observed at  $r = 2.08 \text{ Å}$  and the apparent splitting at  $r = 3.96 \text{ Å}$  to  $4.15 \text{ Å}$ . In

other fluorides, Sn adopts short Sn–F distances (e.g., 2.28 Å in tetragonal BaSnF<sub>4</sub> [94], and as short as 2.03 Å in SnF<sub>2</sub> [128]). We therefore provisionally assign the peak at  $r = 2.08$  Å to short Sn–F bonds, which requires that Sn or F, or both species, are displaced from their ideal fluorite positions.

Fig. 3(b) shows the room-temperature <sup>119</sup>Sn Mössbauer spectrum for our c-BaSnF<sub>4</sub> sample. The spectrum features an asymmetric quadrupole doublet with an isomer shift of around 3 mm s<sup>-1</sup>, characteristic of covalently bonded Sn (II), and a large quadrupole splitting parameter ( $\Delta > 1.5$  mm s<sup>-1</sup>), indicating that Sn exhibits a stereoactive lone pair [62, 129]. The experimental spectrum can be reconstructed using two quadrupole doublets with distinct isomer-shift and quadrupole-splitting parameters (see the Supporting Information for details), indicating some degree of variation in Sn–F bonding interactions and in the coordination geometry around individual tin cations.

Dénès and co-workers have previously proposed a structural model for fluorite Ca<sub>1-x</sub>Sn<sub>x</sub>F<sub>2</sub>, on the basis of experimental XRD and Mössbauer data similar to those reported here [62, 87]. In this model, the presence of a tin stereoactive lone pair causes each tin cation to be displaced towards one face of its enclosing [F8] cube, giving square-pyramidal SnF<sub>4</sub>E coordination with a reduced nearest-neighbour Sn–F distance. This structural model at first appears to be consistent with our XRD and Mössbauer data and hence to provide an explanation for the deviation from the ideal fluorite structure evident in the short-range PDF data described above. The position of the first peak in our PDF data, however, at  $r = 2.08$  Å, is too short to be explained by square-pyramidal SnF<sub>4</sub>E coordination within an ideal cubic array of fluoride ions: the shortest possible Sn–F distance from this model is  $a\sqrt{2}/2 = 2.19$  Å. We therefore interpret the PDF feature at  $r = 2.08$  Å as indicative of a significant degree of distortion to the fluorine substructure away from the reference simple-cubic structure. The structural model of Dénès *et al.* also predicts equivalent SnF<sub>4</sub>E coordination for all tin cations, which is inconsistent with the apparent variation in bonding and coordination geometry for tin cations evidenced by the Mössbauer data.

More detail about the local structure of c-BaSnF<sub>4</sub>, including the behaviour of the Sn lone pair, is provided by analysing structures obtained by quenching from an AIMD simulation. Fig. 4 shows a (001) cross-section through the electron localisation function (ELF) [114], calculated for a quenched structure from our AIMD simulation. This cross-section intersects with the Wyckoff 4a positions that are occupied by cations in the perfect fluorite structure. Atoms are visible as regions of non-zero ELF density, and each chemical species, Ba, Sn, and F, has a distinct appearance. Ba are visible as bright symmetric rings that are centered approximately on the 4a positions, indicating that barium sits close to its ideal fluorite position. Sn appear as less bright rings, with a bright eccentric lobe that corresponds to the stereoactive

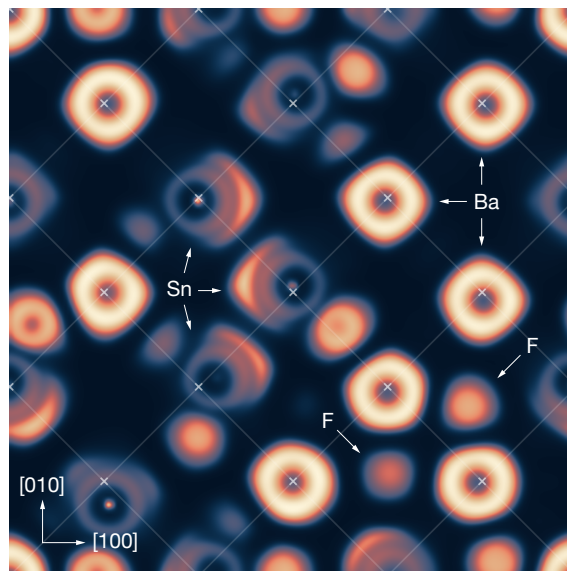


FIG. 4. (001) cross-section through the electron localisation function calculated for c-BaSnF<sub>4</sub> for a single structure quenched from AIMD simulations [114]. Crosses show ideal cation positions ( $Fm\bar{3}m$  Wyckoff 4a) for a fluorite ( $Fm\bar{3}m$ ) structure.

lone pair. These lone pairs are generally oriented approximately along  $\langle 100 \rangle$  directions. The Sn centers appear either to be close to the 4a positions, or, where they are displaced, the displacement appears uncorrelated with the orientation of the lone pair.

We also observe ELF features due to fluoride ions, even though the (001) plane in the figure contains no tetrahedral 8c sites, and therefore should contain no fluoride ions for a perfect fluorite structure. However, we observe a number of fluoride ions occupying either octahedral or tetrahedral-edge positions, showing a high degree of fluoride-ion disorder.

A more quantitative analysis of the c-BaSnF<sub>4</sub> structure is presented in Fig. 5. Fig. 5(a) shows the probability distributions of cation distances from their closest 4a site,  $P[r(M-4a)]$ , for Ba and Sn. Both cation species are, on average, displaced from their corresponding ideal fluorite cation positions, indicating how the cation substructure is locally distorted from a perfect fcc lattice. On average, Sn is displaced further from the nearest 4a position than Ba, which is consistent with the smaller size of Sn. In general, however, the two probability distribution functions have similar shapes, indicating no qualitative difference between Ba positions and Sn positions relative to their formal crystallographic sites.

Fig. 5(b) shows the Ba–F and Sn–F radial distribution functions (RDFs),  $g(r)$ . The nearest neighbour M–F distance is shorter for Sn ( $\sim 2.1$  Å) than for Ba ( $\sim 2.7$  Å), and confirms our earlier assignment of the feature at 2.08 Å in our PDF data (Fig. 3(b)). Integrating these RDFs gives cumulative coordination numbers, which are shown in Fig. 5(c). The coordination number for Ba rises

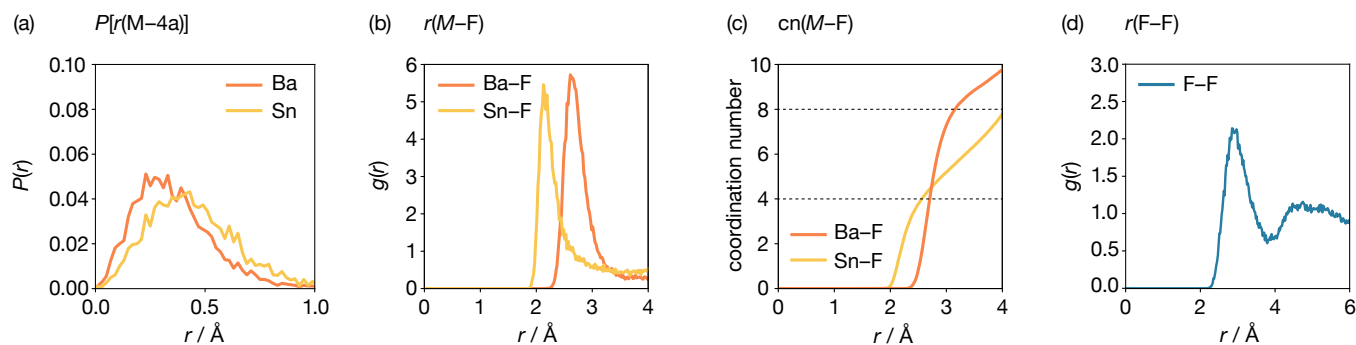


FIG. 5. (a) Probability density functions  $P(r)$ —between Ba and Sn and their respective nearest  $Fm\bar{3}m$  Wyckoff 4a positions. (b)  $M$ -F radial distribution functions ( $M = \{\text{Sn}, \text{Ba}\}$ ). (c)  $M$ -F coordination number functions ( $M = \{\text{Sn}, \text{Ba}\}$ ). The dashed horizontal lines indicate coordination numbers of 4 and 8. (d) F-F radial distribution function.

sharply to  $\sim 8$ , which is the expected number for fluorite-like  $\text{MF}_8$  cation coordination. The coordination number for Sn, however, initially only rises to  $\sim 4$ , indicating that, on average, each Sn has only four neighbouring fluoride ions.

Dénès *et al.* have previously proposed that in  $\text{Ca}_x\text{Sn}_{1-x}\text{F}_2$ , Sn is displaced from the ideal fluorite 4a position towards one face of an enclosing [F8] cube, to accommodate the stereoactive Sn lone pair [62, 87]. For  $c\text{-BaSnF}_4$ , if Sn were sitting off-center in a well-formed [F8] cube then the coordination number would show two distinct steps corresponding to [4+4] coordination. The calculated Sn-F coordination number, however, rises continuously after the first step, reaching  $\sim 8$  at 4 Å: the average coordination environment around Sn includes four neighbouring F that occupy 8c-type positions, with four more F in some diffuse disordered arrangement at distances of 2.3 Å to 4.0 Å. Our data therefore suggest an alternative model for the Sn coordination environment, where the Sn lone pair is accommodated not by Sn being displaced significantly from the 4a position, but instead by a significant disruption of the fluoride ions on the lone-pair-adjacent face of the nominal [F8] coordination environment, which presumably reduces the mutual electrostatic repulsion expected between these fluoride ions and the proximate lone pair [130]. Additional evidence for significant disordering of fluoride ions comes from the F-F RDF (Fig. 5(d)), which shows a very weak second peak, more typical of an amorphous glassy phase than a regular crystalline array of atoms.

Fig. 6 shows a section through the time-average fluoride-ion density calculated from our AIMD simulation. The section is centered on a (001) plane of tetrahedral 8c positions. The superimposed closed and open squares indicate the Ba and Sn atoms, respectively, that tetrahedrally coordinate these 8c positions. The fluoride-ion density is highly heterogeneous and shows stark qualitative differences between Ba-rich regions and Sn-rich regions. In Ba-rich regions, the fluoride-ion density is well localised around the 8c positions, as expected for a conventional fluorite structure. In Sn-rich regions, how-

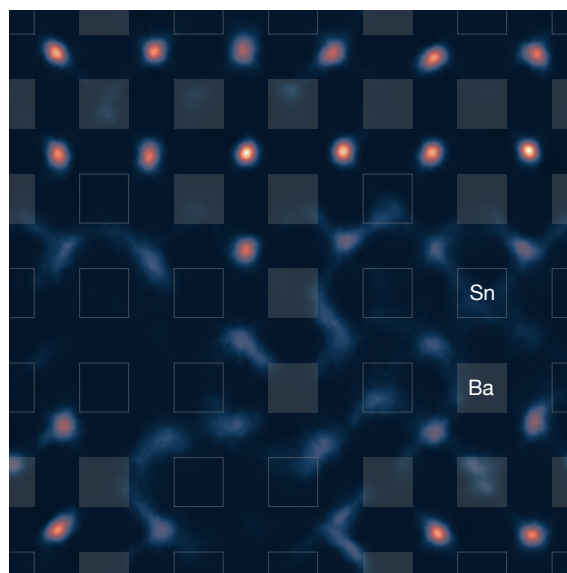


FIG. 6. (001)-projected slice through the time-average fluoride-ion density of  $c\text{-BaSnF}_4$  from AIMD simulation at 600 K, showing a single plane of tetrahedral sites. Each tetrahedral site is coordinated by four cations (cf. Fig. 1(a)), which have their projected positions marked by squares. Filled squares indicate Ba positions and empty squares indicate Sn positions.

ever, the fluoride-ion density is highly diffuse, which is consistent with the proposal above that Sn lone pairs are associated with significant disorder in the local fluoride substructure. These fluoride-ion density data also suggest that the dynamic behaviour of the fluoride ions is strongly dependent on the identity of the nearby cation species: fluoride ions in Ba-rich regions of  $c\text{-BaSnF}_4$  appear to be relatively immobile, while fluoride ions in Sn-rich regions appear to be much more mobile, and we return to this point below.

To obtain another perspective on the degree of fluoride ion disorder, we project the instantaneous fluoride-ion positions from our AIMD simulation trajectory onto



discrete tetrahedral or octahedral sites, defined by the set of Wyckoff 4a sites that define their vertices. This site-projection gives a remarkable 1/3 of fluoride ions occupying octahedral “interstitial” sites rather than conventional tetrahedral sites—i.e., individual octahedral sites are, on average, equally likely to be occupied by fluoride ions than individual tetrahedral sites. This degree of fluoride-ion site-disorder is even greater than the “massive disorder” found in  $\text{RbBiF}_4$  [131], where 1/4 of fluoride ions occupy nominally octahedral positions [132]. Furthermore, this disorder is not simply a large number of thermally generated anion “Frenkel pairs”: quenching from our AIMD simulation produces a 0 K structure with this same proportion of fluoride ions occupying octahedral sites that is 16.7 meV/atom lower in energy than the corresponding optimised structure with all fluoride ions occupying tetrahedral positions. This extreme fluoride-ion disorder is therefore *intrinsic* to  $\text{c-BaSnF}_4$ .

Fig. 7(a,b) shows the probability distribution (number frequency) of tetrahedral and octahedral sites in our AIMD simulation, subclassified by the number of Ba and Sn cations that coordinate each site. These figures also show the proportion of time during the simulation, or probability, that each type of site is occupied by a fluoride ion. For the tetrahedral sites, the occupation probability depends strongly on the identity of the coordinating cations: as the number of coordinating Sn increases the probability of that site type being occupied by fluoride decreases. Comparing the limiting cases of exclusive Ba-coordination and exclusive Sn-coordination,  $\text{Ba}_4$ -coordinated sites are occupied nearly 100% of the time, while  $\text{Sn}_4$ -coordinated sites are nearly always vacant (raw numerical data are available in the Supporting Information). In contrast, for octahedral sites, the occupation probability depends much less strongly on the identity of the coordinating cations; each type of octahedral site is occupied approximately 2/3 of the time, although we do observe a weak preferential occupation of octahedral sites with equal numbers of coordinating Ba and Sn.

The probability of fluoride-ions occupying a given site can be interpreted as a relative free energy for that site. Fig. 7(c) shows distributions of per-site relative free energies, calculated for each individual tetrahedral and octahedral site as  $\Delta F_{\text{site}} = -kT \ln(P_{\text{occ}})$ , where  $k$  is the Boltzmann constant,  $T$  is the simulation temperature, and  $P_{\text{occ}}$  is the probability of each site being occupied, calculated from the AIMD simulation. These distributions can be thought of as effective “densities-of-states” of the different tetrahedral and octahedral site types. In Fig. 7(c), we also show a vertical line corresponding to the point where 2/3 of all available sites are statistically occupied, assuming that sites are preferentially occupied in order of increasing relative free energy.

In a conventional fluorite, the tetrahedral sites are low energy, and the octahedral “interstitial” sites are higher energy. Moving an anion from a tetrahedral site to an octahedral site increases the total system energy, and forming Frenkel pairs is therefore a thermally activated

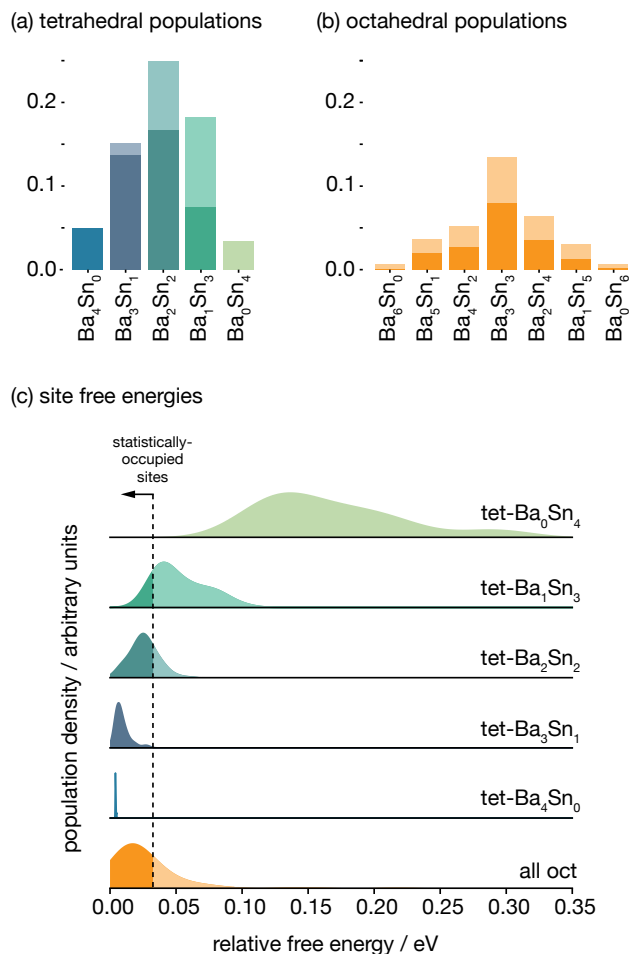


FIG. 7. (a) and (b) (lighter bars) probability distribution (number frequency) of tetrahedral and octahedral sites,  $p(\text{site})$ , in the special-quasi-random AIMD simulation cell, subclassified by the number of Ba and Sn that coordinate each site; (darker bars) joint probabilities for each site type being present in the simulation structure and being occupied by a fluoride ion,  $p(\text{site} \cap \text{occupied})$ , calculated from AIMD simulation. The probability of a given site type being occupied by a fluoride ion,  $p(\text{occupied}|\text{site})$ , is given by the relative proportion of the darker bar to the lighter bar for each site type;  $p(\text{occupied}|\text{site}) = p(\text{site} \cap \text{occupied})/p(\text{site})$ . Numerical data are provided in a table in the Supporting Information. (c) Distributions of site-occupation relative free energies, calculated from AIMD, grouped by fluoride-ion site type. Octahedral sites are shown as a single distribution.

process. Fig. 7(c) illustrates how this conceptual model breaks down in  $\text{c-BaSnF}_4$ , where the relative free energy of tetrahedral sites increases with increasing Sn coordination. For sites with two or more coordinating Sn, some proportion of these sites are spontaneously depopulated, with the corresponding fluoride ions instead preferentially occupying octahedral sites. For  $\text{Ba}_1\text{Sn}_3$ - and  $\text{Sn}_4$ -coordinated tetrahedral sites, this effect is large enough that these sites are nearly fully depopulated, contributing to the high octahedral-site occupation. This behaviour

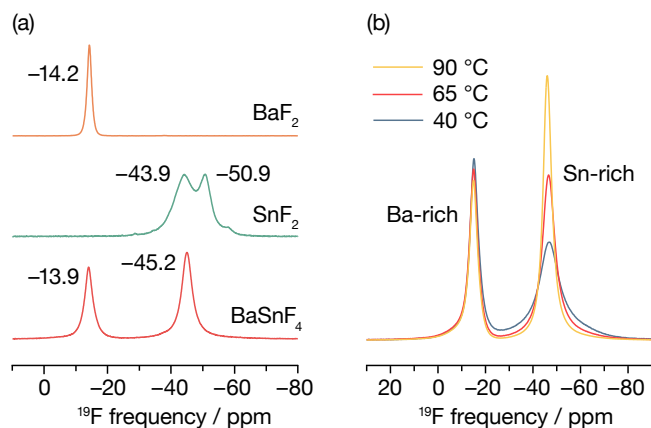


FIG. 8. (a)  $^{19}\text{F}$  MAS (64 kHz) NMR spectra of  $\text{c-BaSnF}_4$  and its precursors  $\text{BaF}_2$  and  $\alpha\text{-SnF}_2$ . (b) Variable-temperature  $^{19}\text{F}$  MAS (30 kHz) of  $\text{c-BaSnF}_4$  recorded at  $40^\circ\text{C}$ ,  $65^\circ\text{C}$  and  $90^\circ\text{C}$ . Fits to these  $\text{c-BaSnF}_4$  spectra are provided in the Supporting Information.

is consistent with a model where Sn lone pairs repel fluoride ions from adjacent tetrahedral sites, forcing these ions to instead occupy octahedral sites. The analysis presented here also indicates that this effect is additive; the more Sn cations coordinating a given tetrahedral site, the stronger the effective repulsion, and the greater the bias to spontaneously depopulate these sites.

### Fluoride-ion dynamics

Having characterised the structure of  $\text{c-BaSnF}_4$ , we now consider the fluoride ion dynamics, and how this is affected by the structural features described above, first using  $^{19}\text{F}$  MAS NMR spectroscopy, and second by further analysis of our AIMD simulations.

In  $M'_xM''_{1-x}\text{F}_2$  mixed-cation fluorites with no stereoactive lone pair, such as  $\text{Ca}_x\text{Ba}_{1-x}\text{F}_2$ ,  $^{19}\text{F}$  MAS NMR spectra show five distinct features corresponding to tetrahedral fluoride environments with different combinations of neighbouring cation species, i.e.  $\text{FM}'_{4-x}\text{M}''_x$  ( $x = \{0, 1, 2, 3, 4\}$ ) [33, 133, 134]. The  $^{19}\text{F}$  MAS NMR spectrum for  $\text{c-BaSnF}_4$  instead shows only two distinct contributions at  $-14$  ppm and  $-45$  ppm (Fig. 8(a)). The first of these peaks has a  $\delta_{\text{iso}}$  value close to that of  $\text{BaF}_2$  ( $-14.2$  ppm), where fluoride ions have occupy  $\text{Ba}_4$ -coordinated tetrahedral sites. The second peak aligns with the average  $\delta_{\text{iso}}$  value of  $\alpha\text{-SnF}_2$  ( $-46$  ppm) [135], in which fluoride is triply coordinated with short Sn–F distances [136]. Based on these comparisons, we assign these features at  $-14$  ppm and  $-45$  ppm to broadly Ba-rich and Sn-rich fluoride environments, respectively. The assignment of fluoride environments into broadly two types is qualitatively consistent with the computational fluoride-ion density data (Fig. 6), where we observe quite different fluoride-ion densities in Ba-rich versus Sn-rich regions of our simulation model.

Our XRD data, above, indicate that Ba and Sn are randomly distributed across the fluorite 4a cation sites, and our AIMD simulations predict a complex fluorine substructure. Both results imply that  $\text{c-BaSnF}_4$  contains a rich variety of fluoride-ion environments, which might be expected to be observable in the experimental  $^{19}\text{F}$  MAS NMR spectrum, as in other mixed-cation fluorites [33]; and yet we observe only two peaks. This apparent contradiction can be reconciled with our expectation of a complex fluorine substructure if we consider fluorine exchange between different sites within the host framework [137]. Fluorine exchange between Ba-rich sites can cause individual peaks associated with different Ba-rich environments to coalesce, giving a single observed resonance. The same reasoning applies to Sn-rich environments, suggesting that they too exhibit fluorine exchange on the NMR timescale.

A third type of fluorine exchange is that between Ba-rich and Sn-rich environments, which we probe using variable-temperature  $^{19}\text{F}$  MAS NMR spectroscopy. Fig. 8(b) shows spectra recorded at  $40^\circ\text{C}$ ,  $65^\circ\text{C}$  and  $90^\circ\text{C}$ . As the temperature increases, the relative intensity of the peak assigned to fluoride ions in Sn-rich environments also increases, from 54% to 60%, at the expense of the peak assigned to fluoride ions in Ba-rich environments, confirming some degree of fluoride-ion exchange between Ba-rich and Sn-rich environments.

For a simple two-site exchange between Ba-rich and Sn-rich environments, increasing temperature would be expected to produce a broadening of the associated resonances before their coalescence into a single resonance with an intermediate chemical shift. We do not observe such behaviour, and instead the peaks assigned to Ba-rich and Sn-rich fluoride environments remain distinct across the investigated temperature range. This behaviour is consistent with only some fraction of fluoride ions in Ba-rich environments undergoing exchange with ions in Sn-rich sites, with this fraction gradually increasing with temperature, and with this Ba-rich–Sn-rich exchange process being slower than exchange between different Sn-rich environments [137]; i.e., on the same timescale of exchange between Ba-rich and Sn-rich environments, fluoride ions in Sn-rich environments undergo exchange between several different Sn-rich environments.

The observation that fluoride ion exchange between Sn-rich environments is much faster than that between Ba-rich environments or between Ba-rich and Sn-rich environments is further supported by the observation of motional narrowing of the Sn-rich peak with increasing temperature, indicating that the so-called fast-exchange regime is reached. This picture of locally inhomogeneous fluoride-ion dynamics is also qualitatively consistent with the time-average fluoride-ion density obtained from AIMD (Fig. 6), where Ba-coordinated regions show highly localised fluoride-ion density, indicative of significantly less mobile ions, while Sn-coordinated regions show diffuse interconnected fluoride-ion density, suggesting more facile fluoride-ion motion between these sites.

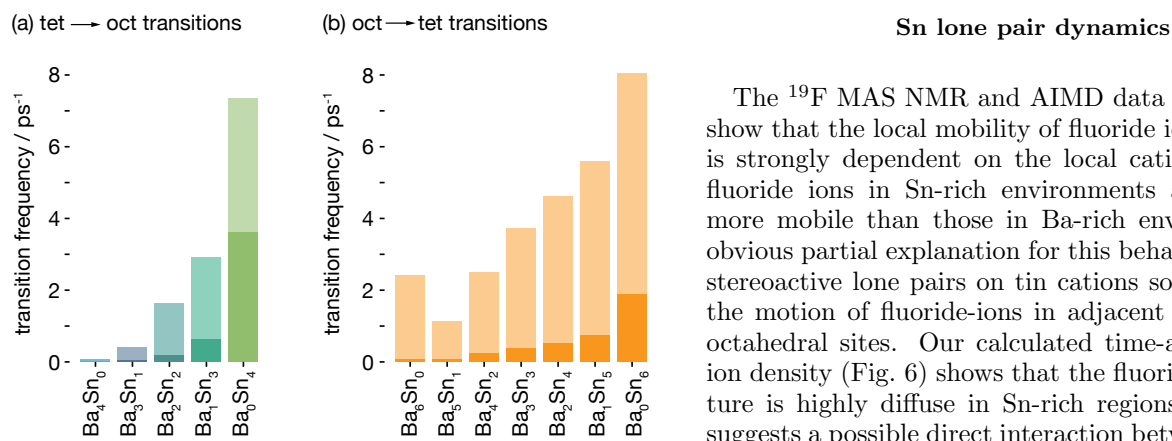


FIG. 9. Site–site transition frequencies for fluoride ions in (a) tetrahedral sites, and (b) octahedral sites, classified according to the cation nearest-neighbours. Transition frequencies are normalised with respect to their time-average occupations, giving frequencies that are equivalent to inverse average site-occupation times. Lighter bars show data for all transitions and darker bars show data only for “non-returning” transitions, as described in the main text.

To validate this model of faster fluoride-ion motion in Sn-rich regions, we performed additional analysis of our AIMD data to calculate site–site transition frequencies for each type of tetrahedral and octahedral site. To estimate the degree to which these fluoride-ion site–site transitions contribute to long-range diffusion, rather than simple back-and-forth motion between adjacent sites, we also calculated frequencies of “non-returning” transitions; these are transitions between two sites,  $1 \rightarrow 2$ , where the next transition made by the mobile ion takes it to a third site,  $1 \rightarrow 2 \rightarrow 3$ , rather than returning it to the original site,  $1 \rightarrow 2 \rightarrow 1$ .

The calculated site–site transition frequencies for tetrahedral and octahedral sites as a function of their Ba/Sn coordination are shown in Fig. 9, normalised by the proportion of time each site type is occupied—this normalisation gives transition frequencies that are equivalent to average inverse residence times; higher transition frequencies correspond to fluoride ions leaving a particular site more quickly. The calculated site–site transition frequencies for both tetrahedral and octahedral sites generally increase with increasing degree of Sn-coordination, with this effect particularly strong for the tetrahedral sites. These data from AIMD simulation, therefore, are consistent with the model inferred from the variable-temperature NMR and fluoride-ion time-average density data (Figs. 6 & 8(b)): fluoride ions in “Sn-rich” sites are, in general, more mobile than fluoride ions in “Ba-rich” sites. We also note that the site-occupation–normalised transition frequencies are much higher for Ba-rich octahedral sites than for Ba-rich tetrahedral sites, which speaks to the relative stability of tetrahedral sites compared to octahedral sites in Ba-rich regions.

The <sup>19</sup>F MAS NMR and AIMD data presented above show that the local mobility of fluoride ions in c-BaSnF<sub>4</sub> is strongly dependent on the local cation composition: fluoride ions in Sn-rich environments are significantly more mobile than those in Ba-rich environments. An obvious partial explanation for this behaviour is that the stereoactive lone pairs on tin cations somehow promote the motion of fluoride-ions in adjacent tetrahedral and octahedral sites. Our calculated time-average fluoride-ion density (Fig. 6) shows that the fluoride-ion substructure is highly diffuse in Sn-rich regions, which further suggests a possible direct interaction between the Sn lone pairs and the mobile fluoride ions.

To quantify the degree of spatial correlation between the Sn lone pairs and nearby fluoride ions, we have calculated the lone-pair–fluoride-ion polar spatial distribution function  $g(r, \theta)$  (Fig. 10). This distribution function describes the time-average fluoride-ion coordination environment around tin, as a function of distance from the central tin cation,  $r$ , and the angle between the Sn–F vector and the lone-pair–orientation vector,  $\theta$ . On the reverse side of the central tin from the lone-pair, there is a clear feature at  $r = 2.1 \text{ \AA}$  with maximum intensity at  $135^\circ$ , i.e., the position of the tetrahedral 8c site if the lone pair is oriented towards the center of the opposite cube-face. On the lone-pair side, however, there is a distinct lack of structure, and fluoride density is instead smeared out in a broad region from  $r > 3 \text{ \AA}$ . This distribution function is consistent with the model proposed from inspection of the time-average fluoride-ion density plot (Fig. 6): the Sn lone pair is preferentially oriented towards one face of the enclosing cubic site, and fluoride ions that would occupy the corners of this face in a perfect fluorite structure are repelled by the lone pair, which strongly disrupts the fluoride structure in the vicinity of the lone pair.

Another notable feature of the lone-pair–fluoride-ion spatial distribution function is that the intense feature corresponding to fluoride ions occupying tetrahedral sites is angularly diffuse. While some of this effect can be attributed to movement of these fluoride ions within their tetrahedral sites, it would be surprising for such movement to preserve the Sn–F separation. An alternative process that provides an explanation for the angular form of this feature is that the tin lone pair is reorienting relative to the reference fluorite lattice on a simulation timescale. To quantify any lone-pair reorientation dynamics, we calculated the Sn-dipole orientational autocorrelation function  $\langle \hat{\mu}(0) \cdot \hat{\mu}(t) \rangle$ , which describes the average change in relative orientation of the stereoactive lone pairs in time  $t$ . This autocorrelation function (Fig. 11) shows a clear decay on a picosecond timescale, showing that tin lone pairs in c-BaSnF<sub>4</sub> undergo dynamic reorientation.

The Sn-dipole orientational autocorrelation function does not decay to zero. Therefore, on average, the orien-

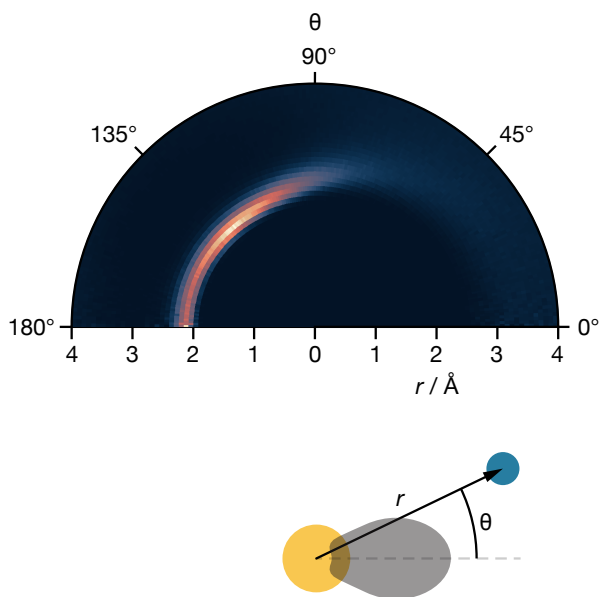


FIG. 10. Sn-lone-pair-fluoride-ion polar spatial distribution function,  $g(r, \theta)$ , for  $c\text{-BaSnF}_4$ , calculated from AIMD simulation.

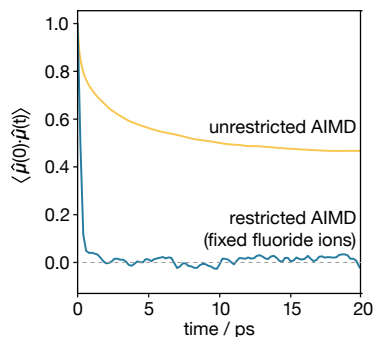


FIG. 11. Sn-dipole orientational autocorrelation function for  $c\text{-BaSnF}_4$ , for unrestricted AIMD, and for AIMD with fixed-position fluoride ions.

tation of each tin lone pair is biased, with the lone pair more likely to point in one particular direction than in another. Plotting individual dipole-orientation autocorrelation functions for each lone pair (see the Supporting Information) shows that the strength of this bias varies significantly across tins, indicating that the degree of orientational bias is sensitive to the local tin environment.

To probe the degree to which the local tin environment directs the orientational bias for individual tin lone pairs, we calculated, for each lone pair, the proportion of time that this lone pair points towards each face of the enclosing cubic site. Each Sn has 12 cation nearest-neighbours arranged in a cuboctahedron. For a given  $\{001\}$  vector from the central Sn, four of these cations are in front of the central Sn, and coordinate the fluoride sites on the front-face of the Sn 4a site, and four of these cations are

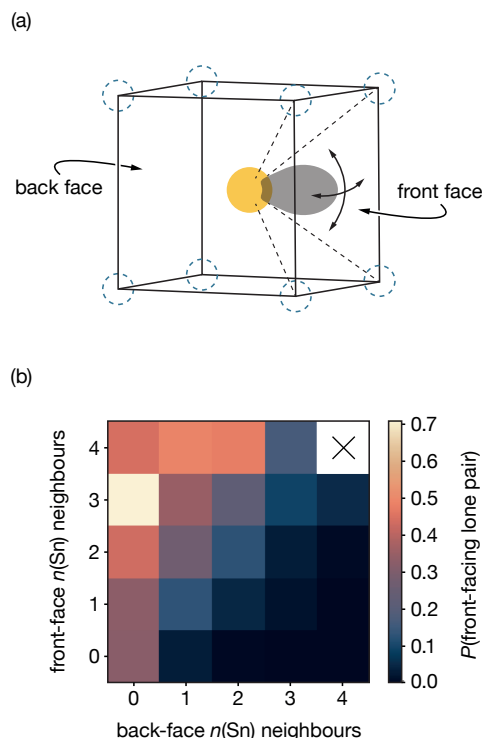


FIG. 12. (a) Schematic of a Sn lone pair oriented towards one face of the cubic cation site. We consider a lone pair to be oriented towards a given face if the Sn dipole vector falls inside the square pyramid formed by the central Sn and the four corresponding vertex 8c positions. (b) Heat-map for the proportion of time that a Sn lone pair is oriented towards a particular face of the cubic cation site, as a function of the number of nearest-neighbour tins in the  $\{001\}$  plane adjacent to the front-face of the cubic site (with respect to the lone pair orientation) and the number of nearest-neighbour tins in the plane  $\{001\}$  plane adjacent to the back-face of the cubic site (with respect to the lone pair orientation).

behind the central Sn, and coordinate the fluoride sites on the back-face of the Sn 4a site—the other four neighbouring cations occupy the same  $\{001\}$  plane as the central Sn. Because the local fluorine environment depends on the arrangement of the nearby Sn and Ba cations (as shown above; Fig. 6), we consider the numbers of Ba and Sn cations coordinating the front-face and back-face of each tin as an effective descriptor for the degree to which a particular tin has a symmetric or asymmetric local coordination environment.

In Fig. 12(b) we show the proportion of time a lone pair points towards a given face of the enclosing cubic site, as a function of the number of nearest-neighbour Sn (out of a maximum of 4) that coordinate the front-face 8c sites and the number of nearest-neighbour Sn (again out of a maximum of 4) that coordinate the back-face 8c sites, with the data presented as a heat map. Data on the diagonal where  $n(\text{Sn})_{\text{front}} = n(\text{Sn})_{\text{back}}$  correspond to lone pair orientations with symmetric front-face-back-face nearest-neighbour cation environments.

These data all show relatively low values, indicating that lone pair orientations with balanced cation coordination are weakly or negligibly biased. In contrast, lone pair orientations with more front-face Sn neighbours than back-face Sn neighbours show a strong bias. As a consequence, the stereoactive Sn lone pairs in *c*-BaSnF<sub>4</sub>, on average, tend to point towards other nearby tins. Clusters of Sn cations are therefore expected to have all their lone pairs preferentially oriented towards the interior of the cluster, giving a cooperative effect where these Sn lone pairs all disrupt any fluoride ion occupation of mutually coordinated tetrahedral sites. This model is consistent with the increasing tetrahedral site free energy with increasing Sn-coordination (Fig. 7) and provides an explanation for the extreme disruption of the fluoride substructure in Sn-rich regions, as observed in the fluoride-ion time-average density (Fig. 6).

The timescale for lone-pair reorientation is similar to the timescale of fluoride-ion site-site transitions, which suggests possible coupling between these two kinds of dynamics. To examine whether the fluoride ion dynamics and lone pair dynamics are, in fact, coupled, we performed an additional AIMD simulation with all fluoride ions fixed at their ideal fluorite positions, and calculated the corresponding Sn-dipole orientational autocorrelation function. With the fluoride ions fixed, the lone-pair orientational autocorrelation function decorrelates on a sub-picosecond timescale (Fig. 11), decaying to a rotationally symmetric (unbiased) value of zero.

This rapid decay of the Sn-dipole orientational autocorrelation function when the fluoride positions are fixed suggests that fluoride-ion dynamics and lone pair dynamics are strongly coupled. When the fluoride ions are fixed to their 8c lattice positions, the lone pair moves freely—no matter which direction it points in there is a strong lone-pair–fluoride repulsion. When the fluoride ions are free to move, however, a number of these fluoride ions move from unstable tetrahedral sites into more favourable octahedral sites, leaving vacant tetrahedral sites next to tin. The Sn lone pair preferentially orients towards these vacant sites to minimise the lone-pair–fluoride-ion repulsion (Fig. 10). As fluoride ions move between sites, the Sn lone pairs dynamically reorient in concert with the changing local fluoride ion configuration, giving strong coupling between the fluoride-ion dynamics and the lone-pair reorientation dynamics.

## SUMMARY AND CONCLUSIONS

To develop solid electrolytes with high ionic conductivities it is necessary to understand how the chemistry of the host framework modulates the structure and dynamics of the mobile ion species [27, 28, 138, 139]. In many families of solid electrolytes, introducing compositional or structural disorder within the host framework is an effective strategy for increasing ionic conductivity [10, 15, 22–30]. (M, Sn)F<sub>2</sub> fluorites have previously

been proposed to exhibit two distinct forms of host-framework disorder [62, 87–89]: cation–site-occupation disorder, where the two cationic species are distributed randomly over the available sites; and Sn–lone-pair orientational disorder, where Sn exhibits stereoactive lone pairs with random orientations. This proposed coexistence of two distinct forms of host-framework disorder makes (M, Sn)F<sub>2</sub> fluorites a particularly focus of study in the context of understanding the possible interplay between disorder types, and how, together, they modulate ion transport.

Here, we have investigated the structure and fluoride-ion dynamics of the cation-disordered fluorite cubic (*c*-)BaSnF<sub>4</sub>. Rietveld refinement of XRD data confirms an average fluorite structure with {Ba,Sn} disorder (Fig. 2). <sup>119</sup>Sn Mössbauer spectroscopy demonstrates the presence of stereoactive Sn(II) lone pairs, and total-scattering PDF data show clear deviations from the average fluorite structure at short range (Fig. 3).

Using *ab initio* molecular dynamics (AIMD) simulations, we have shown that the fluorine substructure in *c*-BaSnF<sub>4</sub> is highly inhomogeneous and depends strongly on the local cationic composition (Fig. 4 and Fig. 6). In Ba-rich regions, the fluoride ions occupy fluorite-like tetrahedrally-coordinated sites that form [F8] cubes around barium. In Sn-rich regions, in contrast, the fluoride-ion substructure is highly diffuse, with fluoride ions displaced from tetrahedral sites adjacent to tin into octahedral “interstitial” sites.

We attribute the displacement of fluoride ions from tin-adjacent tetrahedral sites into octahedral interstitial sites to the presence of the stereoactive lone pair on the tin cations. The tin cations sit relatively close to their ideal fluorite positions, and exhibit highly eccentric charge distributions that are characteristic of a stereoactive lone pair, in agreement with our <sup>119</sup>Sn Mössbauer data. This lone-pair charge density destabilises fluoride ions occupying adjacent tetrahedral sites, in effect pushing these fluoride ions into octahedral sites, thereby strongly disrupting the fluoride-ion substructure. This effect is clearly seen in the Sn–lone-pair–fluoride-ion polar spatial distribution function (Fig. 10), where fluoride ions on the back face of Sn sites—i.e., the opposite side from the lobe of the lone pair—are well structured, while fluoride ions on the front face of Sn sites—in the direction the lone pair is oriented—are strongly repelled and highly disordered.

As a consequence of this Sn–lone-pair–fluoride-ion repulsion, *c*-BaSnF<sub>4</sub> exhibits a remarkable concentration of “interstitial” fluoride ions that occupy octahedral sites. In our simulations, 1/3 of fluoride ions occupy octahedral sites, making it equally likely that, on average, octahedral sites and tetrahedral sites are occupied by fluoride ions. This level of octahedral-site occupation exceeds that of previously reported “massively disordered” fluorites, such as RbBiF<sub>4</sub> [131], where 1/4 of fluoride ions occupy octahedral sites [132]. In *c*-BaSnF<sub>4</sub> this extreme fluoride-ion disorder is a consequence of a high relative free energy of occupation for tetrahedral sites adjacent to

tin centers and an associated low relative free energy of occupation for octahedral sites (Fig. 7), which is a consequence of the mutual repulsion between Sn–lone-pairs and fluoride ions in adjacent tetrahedral sites.

We have also directly probed fluoride ion dynamics and the effect of cation disorder using variable-temperature  $^{19}\text{F}$  MAS NMR experiments and additional analysis of our AIMD data. Our NMR data show that fluoride ions in  $c\text{-BaSnF}_4$  can be broadly categorised as residing in either “Ba-rich” or “Sn-rich” environments, with fluoride ions in Sn-rich environments more mobile than fluoride ions in Ba-rich environments. This picture of cation-environment-dependent fluoride-ion dynamics is corroborated by our AIMD simulations: calculated site–site transition frequencies are higher for sites with a higher proportion of coordinating tin, showing a direct relationship between the local cation configuration and local anion dynamics.

Our AIMD simulations also reveal that the tin lone pairs dynamically reorient on a picosecond timescale (Fig. 11). By comparing the results from our unrestricted AIMD simulations to equivalent data from simulations where the fluoride ions are fixed to their ideal fluorite positions, we have shown that orientational dynamics of the tin lone pairs is coupled to the dynamics of the nearby fluoride ions. This effect is modulated by the local cation arrangement: for tins with an asymmetric Sn/Ba nearest-neighbour configuration, the tin lone pair preferentially orients in the direction of other, nearby, tins. Hence, clusters of tin cations exhibit a cooperative effect where by the lone pairs on each tin tend to orient towards the interior of this cluster. This cooperative effect explains the dramatic disruption of the fluoride ion substructure in regions where several Sn cations are clustered together (Fig. 6).

The measured room-temperature ionic conductivity of  $c\text{-BaSnF}_4$  ( $4.6 \times 10^{-3} \text{ S cm}^{-1}$ ) is significantly higher than that of, for example, fluorite-structured  $\text{BaF}_2$  [24], which is consistent with the general observation that within structurally-related families of solid electrolytes, host-framework disorder is often correlated with increased ionic conductivities [10, 15, 22–30]. In other materials, this relationship between host-framework disorder and ionic conductivity has been explained as a consequence of a concomitant disordering of the mobile ion species that promotes ion transport [10], or of a reduction in differences in site-occupation energies between mobile-ion sites that flattens the mobile-ion potential energy surface [15]. Our results for  $c\text{-BaSnF}_4$  are consistent with both of these conceptual models: in Sn-rich regions of the structure, the fluoride-ion density is highly diffuse (Fig. 6), indicating significant local fluoride-ion disorder—which is also evident from our calculated F–F radial distribution function, Fig. 5(d)—while our site-occupation analysis shows a destabilisation of Sn-coordinated tetrahedral sites and a stabilisation of octahedral sites that gives overlapping tetrahedral and octahedral site energies (Fig. 7).

Given that  $c\text{-BaSnF}_4$  exhibits such a high degree of fluoride-ion disorder, it is perhaps surprising that it does not have an even higher ionic conductivity. We observe greater fluoride-ion site-disorder (1/3 of fluoride ions occupying octahedral sites) than in the mixed-valence mixed-cation fluorite  $\text{RbBiF}_4$  (1/4 of fluoride ions occupying octahedral sites), which would seem to predict a higher ionic conductivity for  $c\text{-BaSnF}_4$  than for  $\text{RbBiF}_4$ . The room-temperature ionic conductivity of  $\text{RbBiF}_4$ , however, is  $\times 10^2$  greater than that of  $c\text{-BaSnF}_4$  [82]. This result can be explained by recognising that fast-ion transport in solid electrolytes requires not only that there is a small, or non-existent, energy gap between occupied and unoccupied sites, but also that these “frontier” sites form a contiguous percolating diffusion pathway through the material [15]. In  $c\text{-BaSnF}_4$ , the combined effects of cation disorder and lone-pair–fluoride-ion repulsion produce a large spread in tetrahedral site energies (Fig. 7), causing tetrahedral sites with either high-Ba-coordination or high-Sn-coordination to be largely unavailable for long-range fluoride-ion diffusion. Highly-Ba-coordinated tetrahedral sites (e.g.,  $\text{Ba}_4$ ) have low site energies, are nearly fully occupied, and have low site–site transition frequencies, and fluoride ions occupying these sites are therefore largely immobile. As such, clusters of barium cations are expected to obstruct long-range fluoride ion diffusion. Highly-Sn-coordinated tetrahedral sites (e.g.,  $\text{Sn}_4$ ) have a similar blocking effect on diffusion, but for the opposite reason; these sites have high site energies and are therefore rarely occupied, despite having very high site–site transition frequencies. As a result, these Sn-coordinated sites obstruct long-range fluoride ion diffusion by acting as high-energy bottlenecks. The remaining mixed-coordination tetrahedral sites (e.g.,  $\text{Ba}_2\text{Sn}_2$ ) then form a tortuous diffusion pathway, resulting in a lower macroscopic ionic conductivity than might be expected on the basis of local site–site transition frequencies or purely from the high level of fluoride ion disorder present in the structure.

The results presented here demonstrate the complex interplay between two distinct forms of host-framework disorder—cationic site-occupation disorder and lone-pair orientational disorder—and the structure and dynamics of the mobile ion species within a fluoride-ion-conducting solid electrolyte. The complex nature of these interacting effects suggests that the resulting effect on mobile-ion dynamics is likely to be highly dependent on the exact composition and structure of the solid electrolyte, and we expect further exploration of the coupling between crystallographic disorder, lone pair dynamics, and ionic conductivity in solid electrolytes to be a fertile area for future research.

### Supporting Information

Supporting Information: Full EDX analysis data; Temperature-dependent ionic-conductivity data; X-ray

PDF data  $12 \text{ \AA} \leq r \leq 50 \text{ \AA}$ ; Mössbauer hyperfine parameters;  $^{19}\text{F}$  MAS NMR data; Sn-dipole orientational autocorrelation function data (PDF).

### Data and Code availability

A complete dataset for the computational modelling and analysis described in this paper is available from the University of Bath Research Data Archive [140]. This dataset contains inputs and outputs for all DFT calculations, plus scripts for analysis of the DFT data and for plotting Figs. 4, 5, 6, 7, 9, 10, 11 and 12(b). A subsidiary dataset containing only the figure-plotting scripts and relevant input data is available on GitHub [141].

### ACKNOWLEDGEMENTS

B.M., C.M., and D.D. thank the French National Research Agency (STORE-EX Labex Project ANR-10-LABX-76-01) for financial support. D.D. wishes to thank A. Abouerie (funded by the INC-CNRS Emergence program) for conducting preliminary experiments. The work done at the Advanced Photon Source, an Office of Science User Facility operated for the U.S. Department of Energy (DOE) Office of Science by Argonne National Laboratory, was supported by the U.S. DOE under Contract No. DE-AC02-06CH11357. S.W.C. and B.J.M. thank the Faraday Institution CATMAT project (EP/S003053/1, FIRG016) for financial support. This work used the Michael computing cluster (FIRG030), the ARCHER2 UK National Supercomputer Service, with access provided by our membership of the UK's HPC Materials Modelling Consortium (EP/R029431), and the Isambard 2 UK National Tier-2 HPC Service operated by GW4 and the UK Met Office, and funded by EPSRC (EP/T022078/1). BJM acknowledges support from the Royal Society (URF\R\191006).

<sup>†</sup> B.M. and S.W.C. contributed equally to this paper.

\* b.j.morgan@bath.ac.uk; damien.dambournet@upmc.fr.

### REFERENCES

- [1] O. Yamamoto, Solid oxide fuel cells: Fundamental aspects and prospects, *Electrochim. Acta* **45**, 2423 (2000).
- [2] J. B. Goodenough and P. Singh, Review—Solid electrolytes in rechargeable electrochemical cells, *J. Electrochem. Soc.* **162**, A2387 (2015).
- [3] J. C. Bachman, S. Muy, A. Grimaud, H.-H. Chang, N. Pour, S. F. Lux, O. Paschos, F. Maglia, S. Lupart, P. Lamp, L. Giordano, and Y. Shao-Horn, Inorganic solid-state electrolytes for lithium batteries: Mechanisms and properties governing ion conduction, *Chem. Rev.* **116**, 140 (2015).
- [4] J. Janek and W. G. Zeier, A solid future for battery development, *Nature Energy* **1**, 16141 (2016).
- [5] T. Famprikis, P. Canepa, J. A. Dawson, M. S. Islam, and C. Masquelier, Fundamentals of inorganic solid-state electrolytes for batteries, *Nature Mater.* **18**, 1278 (2019).
- [6] S. P. Culver, A. G. Squires, N. Minafra, C. W. F. Armstrong, T. Krauskopf, F. Böcher, C. Li, B. J. Morgan, and W. G. Zeier, Evidence for a solid-electrolyte inductive effect in the superionic conductor  $\text{Li}_{10}\text{Ge}_{1-x}\text{Sn}_x\text{P}_2\text{S}_{12}$ , *J. Am. Chem. Soc.* **142**, 21210 (2020).
- [7] M. A. Kraft, S. Ohno, T. Zinkevich, R. Koerver, S. P. Culver, T. Fuchs, A. Senyshyn, S. Indris, B. J. Morgan, and W. G. Zeier, Inducing high ionic conductivity in the lithium superionic argyrodites  $\text{Li}_{6+x}\text{P}_{1-x}\text{Ge}_x\text{S}_5\text{I}$  for all-solid-state batteries, *J. Am. Chem. Soc.* **140**, 16330 (2018).
- [8] X. He, Y. Zhu, and Y. Mo, Origin of fast ion diffusion in super-ionic conductors, *Nature Commun.* **8**, 15893 (2017).
- [9] M. Burbano, D. Carlier, F. Boucher, B. J. Morgan, and M. Salanne, Sparse cyclic excitations explain the low ionic conductivity of stoichiometric  $\text{Li}_7\text{La}_3\text{Zr}_2\text{O}_{12}$ , *Phys. Rev. Lett.* **116**, 135901 (2016).
- [10] B. J. Morgan, Mechanistic origin of superionic lithium diffusion in anion-disordered  $\text{Li}_6\text{PS}_5\text{X}$  argyrodites, *Chem. Mater.* **33**, 2004 (2021).
- [11] K. Kim and D. J. Siegel, Correlating lattice distortions, ion migration barriers, and stability in solid electrolytes, *J. Mater. Chem. A* **7**, 3216 (2019).
- [12] Y. Xiao, K. Jun, Y. Wang, L. J. Miara, Q. Tu, and G. Ceder, Lithium oxide superionic conductors inspired by garnet and NASICON structures, *Adv. Energy Mater.* **11**, 2101437 (2021).
- [13] B. J. Morgan, Understanding fast-ion conduction in solid electrolytes, *Phil. Trans. R. Soc. A* **379**, 20190451 (2021).
- [14] B. C. Wood, J. B. Varley, K. E. Kweon, P. Shea, A. T. Hall, A. Grieder, M. Ward, V. P. Aguirre, D. Rigling, E. L. Ventura, C. Stancill, and N. Adelstein, Paradigms of frustration in superionic solid electrolytes, *Phil. Trans. R. Soc. A* **379**, 20190467 (2021).
- [15] Y. Zeng, B. Ouyang, J. Liu, Y.-W. Byeon, Z. Cai, L. J. Miara, Y. Wang, and G. Ceder, High-entropy mechanism to boost ionic conductivity, *Science* **378**, 1320 (2022).
- [16] S. Wang, Y. Liu, and Y. Mo, Frustration in super-ionic conductors unraveled by the density of atomistic states, *Angew. Chem. Int. Edit.* **62**, e202215544 (2023).
- [17] D. D. Stefano, A. Miglio, K. Robeyns, Y. Filinchuk, M. Lechartier, A. Senyshyn, H. Ishida, S. Spannenberger, D. Prutsch, S. Lunghammer, D. Rettenwander, M. Wilkening, B. Roling, Y. Kato, and G. Hautier, Superionic diffusion through frustrated energy landscape, *Chem* **5**, 2450 (2019).
- [18] K. Jun, Y. Sun, Y. Xiao, Y. Zeng, R. Kim, H. Kim, L. J. Miara, D. Im, Y. Wang, and G. Ceder, Lithium superionic conductors with corner-sharing frameworks, *Nature Mater.* **21**, 924 (2022).
- [19] Y. Wang, W. D. Richards, S. P. Ong, L. J. Miara, J. C. Kim, Y. Mo, and G. Ceder, Design principles for solid-state lithium superionic conductors, *Nature Mater.* **14**, 1026 (2015).

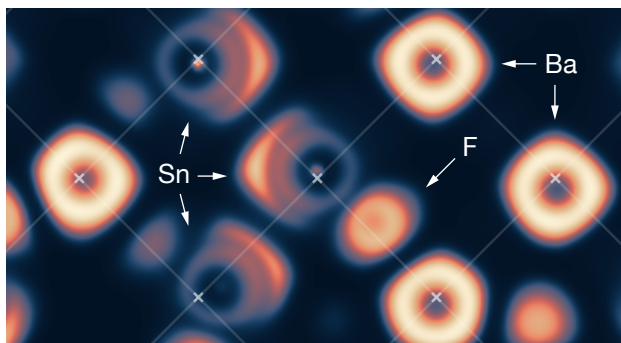
- [20] X. He, Q. Bai, Y. Liu, A. M. Nolan, C. Ling, and Y. Mo, Crystal structural framework of lithium super-ionic conductors, *Adv. Energy Mater.* **9**, 1902078 (2019).
- [21] Z. Zhang, H. Li, K. Kaup, L. Zhou, P.-N. Roy, and L. F. Nazar, Targeting superionic conductivity by turning on anion rotation at room temperature in fast ion conductors, *Matter* **2**, 1667 (2020).
- [22] S. Hull, D. A. Keen, P. A. Madden, and M. Wilson, Ionic diffusion within the  $\alpha^*$  and  $\beta$  phases of  $\text{Ag}_3\text{SI}$ , *J. Phys.: Condens. Matter* **19**, 406214 (2007).
- [23] Y. Zhang, Y. Zhao, and C. Chen, *Ab initio* study of the stabilities of and mechanism of superionic transport in lithium-rich antiperovskites, *Phys. Rev. B* **87**, 134303 (2013).
- [24] A. Düvel, P. Heitjans, P. Fedorov, G. Scholz, G. Cibin, A. V. Chadwick, D. M. Pickup, S. Ramos, L. W. L. Sayle, E. K. L. Sayle, T. X. T. Sayle, and D. C. Sayle, Is geometric frustration-induced disorder a recipe for high ionic conductivity?, *J. Am. Chem. Soc.* **139**, 5842 (2017).
- [25] S. Breuer and M. Wilkening, Mismatch in cation size causes rapid anion dynamics in solid electrolytes: The role of the Arrhenius pre-factor, *Dalton Transactions* **47**, 4105 (2018).
- [26] R. Schlem, S. Muy, N. Prinz, A. Banik, Y. Shao-Horn, M. Zobel, and W. G. Zeier, Mechanochemical synthesis: A tool to tune cation site disorder and ionic transport properties of  $\text{Li}_3\text{MCl}_6$  ( $\text{M} = \text{Y}, \text{Er}$ ) superionic conductors, *Adv. Energy Mater.* **10**, 1903719 (2019).
- [27] A. Gautam, M. Sadowski, M. Ghidui, N. Minafra, A. Senyshyn, K. Albe, and W. G. Zeier, Engineering the site-disorder and lithium distribution in the lithium superionic argyrodite  $\text{Li}_6\text{PS}_5\text{Br}$ , *Adv. Energy Mater.* **11**, 2003369 (2020).
- [28] N. Minafra, M. A. Kraft, T. Bernges, C. Li, R. Schlem, B. J. Morgan, and W. G. Zeier, Local charge inhomogeneity and lithium distribution in the superionic argyrodites  $\text{Li}_6\text{PS}_5\text{X}$  ( $\text{X} = \text{Cl}, \text{Br}, \text{I}$ ), *Inorg. Chem.* **59**, 11009 (2020).
- [29] M. Gombotz, I. Hanghofer, S. Eisbacher-Lubensky, and H. Wilkening, Ionic and electronic transport in the fast Ag conductor  $\alpha^*\text{-Ag}_3\text{SI}$ , *Sol. Stat. Sci.* **118**, 106680 (2021).
- [30] J. Zheng, H. Fang, L. Fan, Y. Ren, P. Jena, and Y. Wu, Antiperovskite  $\text{K}_3\text{OI}$  for K-ion solid state electrolyte, *J. Phys. Chem. Lett.* **12**, 7120 (2021).
- [31] A. R. Symington, J. Purton, J. Statham, M. Molinari, M. S. Islam, and S. C. Parker, Quantifying the impact of disorder on Li-ion and Na-ion transport in perovskite titanate solid electrolytes for solid-state batteries, *J. Mater. Chem. A* **8**, 19603 (2020).
- [32] A. Gautam, M. Sadowski, N. Prinz, H. Eickhoff, N. Minafra, M. Ghidui, S. P. Culver, K. Albe, T. F. Fässler, M. Zobel, and W. G. Zeier, Rapid crystallization and kinetic freezing of site-disorder in the lithium superionic argyrodite  $\text{Li}_6\text{PS}_5\text{Br}$ , *Chem. Mater.* **31**, 10178 (2019).
- [33] A. Düvel, B. Ruprecht, P. Heitjans, and M. Wilkening, Mixed alkaline-earth effect in the metastable anion conductor  $\text{Ba}_{1-x}\text{Ca}_x\text{F}_2$  ( $0 \leq x \leq 1$ ): Correlating long-range ion transport with local structures revealed by ultrafast  $^{19}\text{F}$  MAS NMR, *J. Phys. Chem. C* **115**, 23784 (2011).
- [34] L. Haarmann and K. Albe, From ionic to superionic conductivity: The influence of cation order on sodium diffusion in  $\text{Na}_3\text{Zr}_2\text{Si}_2\text{PO}_{12}$ , *Sol. Stat. Ionics* **363**, 115604 (2021).
- [35] K. Hogrefe, N. Minafra, I. Hanghofer, A. Banik, W. G. Zeier, and H. M. R. Wilkening, Opening diffusion pathways through site disorder: The interplay of local structure and ion dynamics in the solid electrolyte  $\text{Li}_{6+x}\text{P}_{1-x}\text{Ge}_x\text{S}_5\text{I}$  as probed by neutron diffraction and NMR, *J. Am. Chem. Soc.* **144**, 1795 (2022).
- [36] I. Hanghofer, M. Brinek, S. L. Eisbacher, B. Bitschnau, M. Volck, V. Hennige, I. Hanzu, D. Rettenwander, and H. M. R. Wilkening, Substitutional disorder: structure and ion dynamics of the argyrodites  $\text{Li}_6\text{PS}_5\text{Cl}$ ,  $\text{Li}_6\text{PS}_5\text{Br}$  and  $\text{Li}_6\text{PS}_5\text{I}$ , *Phys. Chem. Chem. Phys.* **21**, 8489 (2019).
- [37] A. E. Maughan, Y. Ha, R. T. Pekarek, and M. C. Schulze, Lowering the activation barriers for lithium-ion conductivity through orientational disorder in the cyanide argyrodite  $\text{Li}_6\text{PS}_5\text{CN}$ , *Chem. Mater.* **33**, 5127 (2021).
- [38] F. Wang, H. A. Evans, K. Kim, L. Yin, Y. Li, P.-C. Tsai, J. Liu, S. H. Lapidus, C. M. Brown, D. J. Siegel, and Y.-M. Chiang, Dynamics of hydroxyl anions promotes lithium ion conduction in antiperovskite  $\text{Li}_2\text{OHCl}$ , *Chem. Mater.* **32**, 8481 (2020).
- [39] Z. Zhang and L. F. Nazar, Exploiting the paddle-wheel mechanism for the design of fast ion conductors, *Nature Rev. Mater.* **7**, 389 (2022).
- [40] T. Scholz, C. Schneider, M. W. Terban, Z. Deng, R. Eger, M. Etter, R. E. Dinnebier, P. Canepa, and B. V. Lotsch, Superionic conduction in the plastic crystal polymorph of  $\text{Na}_4\text{P}_2\text{S}_6$ , *ACS Energy Lett.* **7**, 1403 (2022).
- [41] J. G. Smith and D. J. Siegel, Ion migration mechanisms in the sodium sulfide solid electrolyte  $\text{Na}_{3-x}\text{Sb}_{1-x}\text{W}_x\text{S}_4$ , *Chem. Mater.* **34**, 4166 (2022).
- [42] M. K. Gupta, J. Ding, N. C. Osti, D. L. Abernathy, W. Arnold, H. Wang, Z. Hood, and O. Delaire, Fast Na diffusion and anharmonic phonon dynamics in superionic  $\text{Na}_3\text{PS}_4$ , *Energy Environ. Sci.* **14**, 6554 (2021).
- [43] P.-C. Tsai, S. Mair, J. Smith, D. M. Halat, P.-H. Chien, K. Kim, D. Zhang, Y. Li, L. Yin, J. Liu, S. H. Lapidus, J. A. Reimer, N. P. Balsara, D. J. Siegel, and Y.-M. Chiang, Double paddle-wheel enhanced sodium ion conduction in an antiperovskite solid electrolyte, *Adv. Energy Mater.* **13**, 2203284 (2022).
- [44] M. Jørgensen, P. T. Shea, A. W. Tomich, J. B. Varley, M. Berx, S. Lovera, R. Černý, W. Zhou, T. J. Udovic, V. Lavallo, T. R. Jensen, B. C. Wood, and V. Stavila, Understanding superionic conductivity in lithium and sodium salts of weakly coordinating *Closo*-hexahalocarborate anions, *Chem. Mater.* **32**, 1475 (2020).
- [45] Z. Zhang, P.-N. Roy, H. Li, M. Avdeev, and L. F. Nazar, Coupled cation–anion dynamics enhances cation mobility in room-temperature superionic solid-state electrolytes, *J. Am. Chem. Soc.* **141**, 19360 (2019).
- [46] G. Laurita and R. Seshadri, Chemistry, structure, and function of lone pairs in extended solids, *Accounts of Chemical Research* **55**, 1004 (2022).
- [47] U. V. Waghmare, N. A. Spaldin, H. C. Kandpal, and R. Seshadri, First-principles indicators of metallicity and cation off-centricity in the IV-VI rocksalt chalcogenides of divalent Ge, Sn, and Pb, *Phys. Rev. B* **67**, 125111 (2003).



- [48] A. Walsh, D. J. Payne, R. G. Egdell, and G. W. Watson, Stereochemistry of post-transition metal oxides: revision of the classical lone pair model, *Chem. Soc. Rev.* **40**, 4455 (2011).
- [49] M. Avdeev, M. Haas, J. Jorgensen, and R. Cava, Static disorder from lone-pair electrons in pyrochlores, *J. Sol. Stat. Chem.* **169**, 24 (2002).
- [50] R. Seshadri, Lone pairs in insulating pyrochlores: Ice rules and high- $k$  behavior, *Sol. Stat. Sci.* **8**, 259 (2006).
- [51] D. H. Fabini, G. Laurita, J. S. Bechtel, C. C. Stoumpos, H. A. Evans, A. G. Kontos, Y. S. Raptis, P. Falaras, A. V. der Ven, M. G. Kanatzidis, and R. Seshadri, Dynamic stereochemical activity of the  $\text{Sn}^{2+}$  lone pair in perovskite  $\text{CsSnBr}_3$ , *J. Am. Chem. Soc.* **138**, 11820 (2016).
- [52] J. Zhang, D. Ishikawa, M. M. Koza, E. Nishibori, L. Song, A. Q. R. Baron, and B. B. Iversen, Dynamic lone pair expression as chemical bonding origin of giant phonon anharmonicity in thermoelectric  $\text{InTe}$ , *Angew. Chem. Int. Edit.* **62**, e202218456 (2023).
- [53] D. H. Fabini, R. Seshadri, and M. G. Kanatzidis, The underappreciated lone pair in halide perovskites underpins their unusual properties, *MRS Bull.* **45**, 467 (2020).
- [54] R. C. Remsing and M. L. Klein, A new perspective on lone pair dynamics in halide perovskites, *APL Mater.* **8**, 050902 (2020).
- [55] V. Carnevali, S. Mukherjee, D. J. Voneshen, K. Maji, E. Guilmeau, A. V. Powell, P. Vaqueiro, and M. Fornari, Lone pair rotation and bond heterogeneity leading to ultralow thermal conductivity in aikinite, *J. Am. Chem. Soc.* **145**, 9313 (2023).
- [56] J. Portier, J. Reau, S. Matar, J. Soubeyroux, and P. Hagenmuller, Advances on fluorine ion conductors, basic and applied research, *Sol. Stat. Ionics* **11**, 83 (1983).
- [57] G. Mairesse, Bismuth-based oxide conductors novel structural and electrical features, in *Fast Ion Transport in Solids* (Springer Netherlands, 1993) pp. 271–290.
- [58] S. Chaudhuri, M. Castiglione, F. Wang, M. Wilson, P. A. Madden, and C. P. Grey, Study of fluoride ion motions in  $\text{PbSnF}_4$  and  $\text{BaSnF}_4$  compounds with molecular dynamics simulation and solid state NMR techniques, *MRS Proc.* **658**, 109 (2000).
- [59] M. J. Castiglione and P. A. Madden, Fluoride ion disorder and clustering in superionic  $\text{PbF}_2$ , *J. Phys.: Condens. Matter* **13**, 9963 (2001).
- [60] S. Chaudhuri, F. Wang, and C. P. Grey, Resolving the different dynamics of the fluorine sublattices in the anionic conductor  $\text{BaSnF}_4$  using high-resolution MAS NMR techniques, *J. Amer. Chem. Soc.* **124**, 11746 (2002).
- [61] G. Dénès, M. C. Madamba, A. Muntasar, A. Peroutka, K. Tam, and Z. Zhu, Fluoride-ion conductors derived from the fluorite type, in *Mössbauer Spectroscopy in Materials Science* (Springer Netherlands, 1999) pp. 25–38.
- [62] G. Dénès, M. C. Madamba, H. Merazig, A. Muntasar, and Z. Zhu, Site distortions created by the stereoactive lone pair of tin(II) in highly symmetric structures, *AIP Conf. Proc.* **1781**, 020006 (2016).
- [63] I. Mohammad, J. Chable, R. Witter, M. Fichtner, and M. A. Reddy, Synthesis of fast fluoride-ion-conductive fluorite-type  $\text{Ba}_{1-x}\text{Sb}_x\text{F}_{2+x}$  ( $0.1 \leq x \leq 0.4$ ): A potential solid electrolyte for fluoride-ion batteries, *ACS Appl. Mater. Interf.* **10**, 17249 (2018).
- [64] M. Faraday, VII. Experimental researches in electricity. — twelfth series, *Phil. Trans. R. Soc.* **128**, 83 (1838).
- [65] M. Anji Reddy and M. Fichtner, Batteries based on fluoride shuttle, *J. Mater. Chem.* **21**, 17059 (2011).
- [66] C. Rongeat, M. A. Reddy, R. Witter, and M. Fichtner, Nanostructured fluorite-type fluorides as electrolytes for fluoride ion batteries, *J. Phys. Chem. C* **117**, 4943 (2013).
- [67] M. A. Nowroozi, I. Mohammad, P. Molaiyan, K. Wissel, A. R. Munnangi, and O. Clemens, Fluoride ion batteries – past, present, and future, *J. Mater. Chem. A* **9**, 5980 (2021).
- [68] S. V. Gopinadh, P. V. Phanendra, B. John, and T. Mercy, Fluoride-ion batteries: State-of-the-art and future perspectives, *Sust. Mater. Technol.* **32**, e00436 (2022).
- [69] A. B. Lidiard, Crystals with the fluorite structure: Electronic, vibrational and defect properties (Oxford University Press, 1974) pp. 101–184.
- [70] G. Jacucci and A. Rahman, Diffusion of  $\text{F}^-$  ions in  $\text{CaF}_2$ , *J. Chem. Phys.* **69**, 4117 (1978).
- [71] A. R. Allnatt, A. V. Chadwick, and P. W. M. Jacobs, A model for the onset of fast-ion conduction in fluorites, *Proc. Roy. Soc. A* **410**, 385 (1987).
- [72] M. J. Gillan, Dynamics of defects in superionic fluorites, *J. Chem. Soc., Faraday Trans.* **86**, 1177 (1990).
- [73] A. D. Franklin, Born model calculation of defect energies in  $\text{CaF}_2$ , *J. Phys. Chem. Sol.* **29**, 823 (1968).
- [74] C. R. A. Catlow and M. J. Norgett, Shell model calculations of the energies of formation of point defects in alkaline earth fluorides, *J. Phys. C: Sol. Stat. Phys.* **6**, 1325 (1973).
- [75] K.-D. Li, H. Xiao, and L. Wang, Computer simulation study of defect formation and migration energy in calcium fluoride, *Nucl. Inst. Methods Phys. Res. B* **266**, 2698 (2008).
- [76] L. N. Patro and K. Hariharan, Fast fluoride ion conducting materials in solid state ionics: An overview, *Sol. Stat. Ionics* **239**, 41 (2013).
- [77] P. Hagenmuller, J. Réau, C. Lucat, S. Matar, and G. Villeneuve, Ionic conductivity of fluorite-type fluorides, *Sol. Stat. Ionics* **3-4**, 341 (1981).
- [78] M. J. Castiglione, M. Wilson, and P. A. Madden, Polarization effects in the simulation of lead (II) fluoride, *J. Phys.: Condens. Matter* **11**, 9009 (1999).
- [79] M. H. Dickens, W. Hayes, M. T. Hutchings, and C. Smith, Investigation of anion disorder in  $\text{PbF}_2$  at high temperatures by neutron diffraction, *J. Phys. C: Sol. Stat. Phys.* **15**, 4043 (1982).
- [80] C. E. Mohn, M. Krynski, W. Kob, and N. L. Allan, Cooperative excitations in superionic  $\text{PbF}_2$ , *Phil. Trans. R. Soc. A* **379**, 20190455 (2021).
- [81] The defect chemistry of  $\beta\text{-PbF}_2$  is complex: above the superionic transition temperature  $T_c = 711$  K, “interstitial” fluoride ions are thought to occupy non-octahedral-site positions as part of various competing anti-Frenkel defect clusters. The interested reader is directed to Ref. 142 and references therein.
- [82] S. Matar, J.-M. Réau, C. Lucat, J. Granec, and P. Hagenmuller, Synthèse et étude des propriétés de conductivité ionique des phases appartenant aux systèmes  $\text{KBiF}_4 - \text{BiF}_3$  et  $\text{RbBiF}_4 - \text{BiF}_3$ , *Mater. Res. Bull.* **15**, 1295 (1980).
- [83] P. A. Cox, C. R. A. Catlow, and A. V. Chadwick, EXAFS and molecular modelling studies of

- Rb<sub>1-x</sub>Bi<sub>x</sub>F<sub>1+2x</sub>, *J. Mater. Sci.* **29**, 2725 (1994).
- [84] T. T. Netshisaulu, A. V. Chadwick, P. E. Ngoepe, and C. R. A. Catlow, Spectroscopic and computer modelling studies of mixed-cation superionic fluorites, *J. Phys.: Condens. Matter* **17**, 6575 (2005).
- [85] A. Düvel, Ionic conductivity and structure of M<sub>1-x</sub>Pb<sub>x</sub>F<sub>2</sub> (M = Ca, Sr, Ba) solid solutions prepared by ball milling, *Dalton Trans.* **48**, 859 (2019).
- [86] C. R. A. Catlow, L. M. Moroney, S. M. Tomlinson, A. V. Chadwick, and G. N. Greaves, An EXAFS study of the effect of temperature on short range ordering in the ionic conductor, RbBiF<sub>4</sub>, in *Springer Proc. Phys.* (Springer Berlin Heidelberg, 1984) pp. 435–438.
- [87] G. Dénès, M. C. Madamba, A. Muntasar, and Z. Zhu, Combined use of Mössbauer spectroscopy and X-ray diffraction for the study of order–disorder in tin(II)-containing fluoride ion conductors, in *Computational Methods and Experiments in Materials Characterisation II*, edited by C. A. Brebbia and A. A. Mammoli (WIT Press, 2005) Chap. 7.10, pp. 279–288.
- [88] G. Dénès, PbSn<sub>4</sub>F<sub>10</sub>: A new disordered fluorite-type fast ion conductor, *J. Sol. Stat. Chem.* **74**, 343 (1988).
- [89] G. Dénès, Y. Yu, T. Tyliczszak, and A. Hitchcock, Sn-*K* and Pb-*L*<sub>3</sub> EXAFS, X-ray diffraction, and <sup>119</sup>Sn Mössbauer spectroscopic studies of ordered β-PbSnF<sub>4</sub> and disordered Pb<sub>1-x</sub>Sn<sub>x</sub>F<sub>2</sub> (*x* = 0.3, 0.4) solid solutions and PbSn<sub>4</sub>F<sub>10</sub>: High performance fluoride ion conductors, *J. Sol. Stat. Chem.* **104**, 239 (1993).
- [90] G. Dénès, J. Pannetier, and J. Lucas, Les fluorures MSnF<sub>4</sub> à structure PbFCl (M = Pb, Sr, Ba), *C. R. Acad. Sc. Paris* **280**, 831 (1975).
- [91] J. Pannetier, G. Dénès, and J. Lucas, MSnF<sub>4</sub> (M = Pb<sup>++</sup>, Ba<sup>++</sup>, Sr<sup>++</sup>): Thermal expansion and phase transitions, *Mater. Res. Bull.* **14**, 627 (1979).
- [92] J. Liu, L. Yi, P. Zeng, C. Zou, X. Chen, X. Tao, X. Liu, L. Yang, Z. Zang, B. Chang, Y. Shen, and X. Wang, Point defect engineering enabled the high ionic conductivity of BaSnF<sub>4</sub> for solid-state fluoride-ion batteries at room temperature, *Energy Fuels* **36**, 15258 (2022).
- [93] X. Lian and M. Salanne, Capturing the interactions in the BaSnF<sub>4</sub> ionic conductor: Comparison between a machine-learning potential and a polarizable force field, *chemRxiv* 10.26434/chemrxiv-2023-s9hjs (2023).
- [94] M. M. Ahmad, Y. Yamane, and K. Yamada, Structure, ionic conduction, and giant dielectric properties of mechanochemically synthesized BaSnF<sub>4</sub>, *J. Appl. Phys.* **106**, 074106 (2009).
- [95] J. Rodríguez-Carvajal, Recent advances in magnetic structure determination by neutron powder diffraction, *Phys. B: Condens. Matter* **192**, 55 (1993).
- [96] P. Thompson, D. E. Cox, and J. B. Hastings, Rietveld refinement of Debye–Scherrer synchrotron X-ray data from Al<sub>2</sub>O<sub>3</sub>, *J. Appl. Cryst.* **20**, 79 (1987).
- [97] Wissenschaftliche Elektronik GmbH, WINNORMOS.
- [98] K. R. Thurber and R. Tycko, Measurement of sample temperatures under magic-angle spinning from the chemical shift and spin-lattice relaxation rate of <sup>79</sup>Br in KBr powder, *J. Mag. Res.* **196**, 84 (2009).
- [99] D. Massiot, F. Fayon, M. Capron, I. King, S. L. Calvé, B. Alonso, J.-O. Durand, B. Bujoli, Z. Gan, and G. Hoatson, Modelling one- and two-dimensional solid-state NMR spectra, *Mag. Res. Chem.* **40**, 70 (2001).
- [100] A. P. Hammersley, ESRF internal report, ESRF97HA02T, “FIT2D: An introduction and overview” (1997).
- [101] P. Juhás, T. Davis, C. L. Farrow, and S. J. L. Billinge, *PDFgetX3*: A rapid and highly automatable program for processing powder diffraction data into total scattering pair distribution functions, *J. Appl. Cryst.* **46**, 560 (2013).
- [102] C. L. Farrow, P. Juhas, J. W. Liu, D. Bryndin, E. S. Božin, J. Bloch, T. Proffen, and S. J. L. Billinge, PDFfit2 and PDFgui: computer programs for studying nanostructure in crystals, *J. Phys.: Condens. Matter* **19**, 335219 (2007).
- [103] G. Kresse and J. Furthmüller, Efficiency of ab-initio total energy calculations for metals and semiconductors using a plane-wave basis set, *Comput. Mater. Sci.* **6**, 15 (1996).
- [104] G. Kresse and J. Furthmüller, Efficient iterative schemes for *ab initio* total-energy calculations using a plane-wave basis set, *Phys. Rev. B* **54**, 11169 (1996).
- [105] G. Kresse and D. Joubert, From ultrasoft pseudopotentials to the projector augmented-wave method, *Phys. Rev. B* **59**, 1758 (1999).
- [106] J. P. Perdew, A. Ruzsinszky, G. I. Csonka, O. A. Vydrov, G. E. Scuseria, L. A. Constantin, X. Zhou, and K. Burke, Restoring the density-gradient expansion for exchange in solids and surfaces, *Phys. Rev. Lett.* **100**, 136406 (2008).
- [107] P. E. Blöchl, Projector augmented-wave method, *Phys. Rev. B* **50**, 17953 (1994).
- [108] M. Ångqvist, W. A. Muñoz, J. M. Rahm, E. Fransson, C. Durniak, P. Rozyczko, T. H. Rod, and P. Erhart, ICET – a Python library for constructing and sampling alloy cluster expansions, *Adv. Theory Simul.* **2**, 1900015 (2019).
- [109] A. Zunger, S.-H. Wei, L. G. Ferreira, and J. E. Bernard, Special quasirandom structures, *Phys. Rev. Lett.* **65**, 353 (1990).
- [110] S.-H. Wei, L. G. Ferreira, J. E. Bernard, and A. Zunger, Electronic properties of random alloys: Special quasirandom structures, *Physical Review B* **42**, 9622 (1990).
- [111] A. S. Keys, L. O. Hedges, J. P. Garrahan, S. C. Glotzer, and D. Chandler, Excitations are localized and relaxation is hierarchical in glass-forming liquids, *Phys. Rev. X* **1**, 021013 (2011).
- [112] F. H. Stillinger and T. A. Weber, Packing structures and transitions in liquids and solids, *Science* **225**, 983 (1984).
- [113] A. Heuer, Exploring the potential energy landscape of glass-forming systems: from inherent structures via metabasins to macroscopic transport, *J. Phys.: Condens. Matter* **20**, 373101 (2008).
- [114] B. Silvi and A. Savin, Classification of chemical bonds based on topological analysis of electron localization functions, *Nature* **371**, 683 (1994).
- [115] N. Marzari, A. A. Mostofi, J. R. Yates, I. Souza, and D. Vanderbilt, Maximally localized Wannier functions: Theory and applications, *Rev. Mod. Phys.* **84**, 1419 (2012).
- [116] G. Pizzi, V. Vitale, R. Arita, S. Blügel, F. Freimuth, G. Géranton, M. Gibertini, D. Gresch, C. Johnson, T. Koretsune, J. Ibañez-Azpiroz, H. Lee, J.-M. Lihm, D. Marchand, A. Marrazzo, Y. Mokrousov, J. I. Mustafa, Y. Nohara, Y. Nomura, L. Paulatto, S. Poncé, T. Ponweiser, J. Qiao, F. Thöle, S. S. Tsirkin, M. Wierzbowska, N. Marzari, D. Vanderbilt, I. Souza,

- A. A. Mostofi, and J. R. Yates, Wannier90 as a community code: new features and applications, *J. Phys.: Condens. Matter* **32**, 165902 (2020).
- [117] L. Bernasconi, M. Wilson, and P. A. Madden, Cation polarizability from first-principles:  $\text{Sn}^{2+}$ , *Comput. Mater. Sci.* **22**, 94 (2001).
- [118] S. W. Coles, REVELSMD.
- [119] B. J. Morgan, SITE-ANALYSIS.
- [120] A. H. Larsen, J. J. Mortensen, J. Blomqvist, I. E. Castelli, R. Christensen, M. Dulak, J. Friis, M. N. Groves, B. Hammer, C. Hargus, E. D. Hermes, P. C. Jennings, P. B. Jensen, J. Kermode, J. R. Kitchin, E. L. Kolsbjerg, J. Kubal, K. Kaasbjerg, S. Lysgaard, J. B. Maronsson, T. Maxson, T. Olsen, L. Pastewka, A. Peterson, C. Rostgaard, J. Schiøtz, O. Schütt, M. Strange, K. S. Thygesen, T. Vegge, L. Vilhelmsen, M. Walter, Z. Zeng, and K. W. Jacobsen, The atomic simulation environment—a Python library for working with atoms, *J. Phys.: Condens. Matter* **29**, 273002 (2017).
- [121] S. P. Ong, W. D. Richards, A. Jain, G. Hautier, M. Kocher, S. Cholia, D. Gunter, V. L. Chevrier, K. A. Persson, and G. Ceder, Python Materials Genomics (pymatgen): A robust, open-source Python library for materials analysis, *Comput. Mater. Sci.* **68**, 314 (2013).
- [122] C. R. Harris, K. J. Millman, S. J. van der Walt, R. Gommers, P. Virtanen, D. Cournapeau, E. Wieser, J. Taylor, S. Berg, N. J. Smith, R. Kern, M. Picus, S. Hoyer, M. H. van Kerkwijk, M. Brett, A. Haldane, J. F. del Río, M. Wiebe, P. Peterson, P. Gérard-Marchant, K. Sheppard, T. Reddy, W. Weckesser, H. Abbasi, C. Gohlke, and T. E. Oliphant, Array programming with NumPy, *Nature* **585**, 357 (2020).
- [123] P. Virtanen, R. Gommers, T. E. Oliphant, M. Haberland, T. Reddy, D. Cournapeau, E. Burovski, P. Peterson, W. Weckesser, J. Bright, S. J. van der Walt, M. Brett, J. Wilson, K. J. Millman, N. Mayorov, A. R. J. Nelson, E. Jones, R. Kern, E. Larson, C. J. Carey, Í. Polat, Y. Feng, E. W. Moore, J. VanderPlas, D. Laxalde, J. Perktold, R. Cimrman, I. Henriksen, E. A. Quintero, C. R. Harris, A. M. Archibald, A. H. Ribeiro, F. Pedregosa, P. van Mulbregt, and SciPy 1.0 Contributors, SciPy 1.0: Fundamental Algorithms for Scientific Computing in Python, *Nature Methods* **17**, 261 (2020).
- [124] D. Borgis, R. Assaraf, B. Rotenberg, and R. Vuilleumier, Computation of pair distribution functions and three-dimensional densities with a reduced variance principle, *Mol. Phys.* **111**, 3486 (2013).
- [125] S. W. Coles, D. Borgis, R. Vuilleumier, and B. Rotenberg, Computing three-dimensional densities from force densities improves statistical efficiency, *J. Chem. Phys.* **151**, 064124 (2019).
- [126] S. W. Coles, E. Mangaud, D. Frenkel, and B. Rotenberg, Reduced variance analysis of molecular dynamics simulations by linear combination of estimators, *J. Chem. Phys.* **154**, 191101 (2021).
- [127] A. S. Radtke and G. E. Brown, Frankdicksonite,  $\text{BaF}_2$ , a new mineral from Nevada, *Am. Mineral.* **59**, 885 (1974).
- [128] R. C. McDonald, H. H. K. Hau, and K. Eriks, Crystallographic studies of tin(II) compounds. I. Crystal structure of tin(II) fluoride,  $\text{SnF}_2$ , *Inorg. Chem.* **15**, 762 (1976).
- [129] G. Dénés, A. Muntasar, M. C. Madamba, and H. Merazig, Tin(II) lone pair stereoactivity: Influence on structures and properties and Mössbauer spectroscopic properties, in *Mössbauer Spectroscopy* (John Wiley & Sons, Inc., 2013) pp. 202–146.
- [130] A direct comparison between our AIMD RDF data and our experimental PDF data is provided in the Supporting Information, along with an analogous comparison for simulation data where the fluoride ions are constrained to their ideal Wyckoff 8c positions.
- [131] C. R. A. Catlow, Atomistic mechanisms of ionic transport in fast-ion conductors, *J. Chem. Soc., Faraday Trans.* **86**, 1167 (1990).
- [132] J. L. Soubeyroux, J. M. Reau, S. Matar, G. Villeneuve, and P. Hagenmuller, Etude par diffraction neutronique des solutions solides  $\text{K}_{1-x}\text{Bi}_x\text{F}_{1+2x}$  et  $\text{Rb}_{1-x}\text{Bi}_x\text{F}_{1+2x}$ , *Sol. Stat. Ionics* **6**, 103 (1982).
- [133] R. E. Youngman and C. M. Smith, Multinuclear NMR studies of mixed  $\text{Ca}_{1-x}\text{Sr}_x\text{F}_2$  crystals, *Phys. Rev. B* **78**, 014112 (2008).
- [134] F. Preishuber-Pflügl and M. Wilkening, Mechanochemically synthesized fluorides: Local structures and ion transport, *Dalton Trans.* **45**, 8675 (2016).
- [135] T. Bräuniger, S. Ghedia, and M. Jansen, Covalent bonds in  $\alpha\text{-SnF}_2$  monitored by  $J$ -couplings in solid-state NMR spectra, *Z. Anorg. Allg. Chem.* **636**, 2399 (2010).
- [136] G. Will and M. O. Bargouth, Neutron diffraction study of  $\beta\text{-SnF}_2$ , *Z. Krist. Cryst. Mater.* **153**, 89 (1980).
- [137] F. Wang and C. P. Grey, Probing the mechanism of fluoride-ion conduction in  $\text{LaF}_3$  and strontium-doped  $\text{LaF}_3$  with high-resolution  $^{19}\text{F}$  MAS NMR, *Chem. Mater.* **9**, 1068 (1997).
- [138] B. Helm, L. M. Gronych, A. Banik, M. A. Lange, C. Li, and W. G. Zeier, Investigating the  $\text{Li}^+$  substructure and ionic transport in  $\text{Li}_{10}\text{GeP}_{2-x}\text{Sb}_x\text{S}_{12}$  ( $0 \leq x \leq 0.25$ ), *Phys. Chem. Chem. Phys.* **25**, 1169 (2023).
- [139] A. Gautam, M. Ghidui, E. Suard, M. A. Kraft, and W. G. Zeier, On the lithium distribution in halide superionic argyrodites by halide incorporation in  $\text{Li}_{7-x}\text{PS}_{6-x}\text{Cl}_x$ , *ACS Appl. Energy Mater.* **4**, 7309 (2021).
- [140] S. W. Coles, Supporting dataset for “dynamic lone pairs and fluoride-ion disorder in cubic- $\text{BaSnF}_4$ ” (2023), awaiting DOI.
- [141] S. W. Coles, Data analysis for “dynamic lone pairs and fluoride-ion disorder in cubic- $\text{BaSnF}_4$ ” (2023), <https://github.com/user200000/data-BaSnF4>.
- [142] S. Hull, Superionics: Crystal structures and conduction processes, *Rep. Prog. Phys.* **67**, 1233 (2004).



TOC Graphic